NOVEL SAR REDUCTION METHODS FOR MAGNETIC RESONANCE IMAGING

A THESIS

SUBMITTED TO THE DEPARTMENT OF ELECTRICAL AND

ELECTRONICS ENGINEERING

AND THE INSTITUTE OF ENGINEERING AND SCIENCES

OF BILKENT UNIVERSITY

IN PARTIAL FULLFILMENT OF THE REQUIREMENTS

FOR THE DEGREE OF

DOCTOR OF PHILOSOPHY

By

Yiğitcan Eryaman

March 2011

I certify that I have read this thesis and that in my opinion it is fully adequate, in scope and in quality, as a thesis for the degree of doctor of philosophy

_____

Prof. Dr. Ergin Atalar (Supervisor)

I certify that I have read this thesis and that in my opinion it is fully adequate, in scope and in quality, as a thesis for the degree of doctor of philosophy

_____

Prof. Dr. Yusuf Ziya İder

I certify that I have read this thesis and that in my opinion it is fully adequate, in scope and in quality, as a thesis for the degree of doctor of philosophy

_____

Prof. Dr. Ayhan Altıntaş

I certify that I have read this thesis and that in my opinion it is fully adequate, in scope and in quality, as a thesis for the degree of doctor of philosophy

_____

Prof. Dr. Murat Eyüboğlu

I certify that I have read this thesis and that in my opinion it is fully adequate, in scope and in quality, as a thesis for the degree of doctor of philosophy

_____

Prof. Dr. Mark Ladd

Approved for the Institute of Engineering and Sciences:

_____

Prof. Dr. Levent Onural

Director of Institute of Engineering and Sciences

ABSTRACT

NOVEL SAR REDUCTION
METHODS FOR MAGNETIC RESONANCE
IMAGING

Yiğitcan Eryaman

Ph.D. in Electronics Engineering

Supervisor: Prof. Dr. Ergin Atalar

March 2011

In this thesis, novel methods are presented, which can be used to reduce the heating of the human body due to radiofrequency fields in magnetic resonance imaging (MRI). The proposed methods depend on the modification of the electric field distribution for reducing the specific absorption rate (SAR). These methods can be used to reduce the local SAR in the vicinity of metallic devices and the whole-volume average SAR, as shown by electromagnetic field simulations and phantom, animal and patient experiments. These results can improve the safety of MRI scans performed on patients with metallic implants and MRI-guided interventional procedures. Additionally, by reducing the whole body average SAR, safer and faster MRI scans can be performed.

ÖZET

MANYETİK REZONANS GÖRÜNTÜLEME'DE ÖZGÜL SOĞRULMA HIZINI AZALTMAK İÇİN YENİ YÖNTEMLER

Yiğitcan Eryaman

Elektrik ve Elektronik Mühendisliği Bölümü Doktora

Tez Yöneticisi: Prof. Dr. Ergin Atalar

Mart 2011

Bu tezde, insan vücudunun Manyetik Rezonans Görüntüleme (MRG) esnasında radyofrekans (RF) alana bağlı ısınmasını azaltmak için kullanılabilecek yeni yöntemler sunulmaktadır. Önerilen yöntemler Özgül Soğrulma Hızı'nın (ÖSH) azaltılması için elektrik alanın değiştirilmesine dayanır. Elektromanyetik benzetimler, fantom, hayvan ve insan deneyleri ile gösterildiği üzere bu yöntemler metal cihazlarin yakinlarinda oluşan yerel ÖSH'nın ve tüm vücut ortalama ÖSH'nın azaltılması için kullanılabilir. Bu sonuçlar vücudunda implant taşıyan hastalarda yapılan MRG taramalarının ve MRG rehberliğindeki girişimsel ugyulamaların güvenliğini arttırabilir. Ayrıca tüm vücut ÖSH'nın azaltılması suretiyle daha güvenli ve hızlı MRG taramaları da yapılabilir.

Anahtar Kelimeler: Manyetik Rezonans Görüntüleme(MRG), Özgül Soğrulma Hızı (ÖSH), implant, radyofrekans(RF) alan

Acknowledgements

Thanks to many people who supported me during the past 4 years of my PhD study. Thanks to them, I was able to continue research persistently, and I was able to finish this thesis which I hope will be a useful source for the future graduate students working in the field of MRI. Among many people, I want to thank first to **Prof. Ergin Atalar** who guided me with his wisdom, experience, and humanity through this exciting journey of science. He is a great mentor and I owe him a debt of gratitude for everything that he taught me.

I also want to thank my jury members, **Prof. Ayhan Altıntaş**, **Prof. Murat Eyüboğlu**, **Prof. Ziya İder** and especially **Prof. Mark Ladd** who came from Germany to attend my jury. Their valuable comments improved the scientific quality of this thesis.

I want to thank my friends in National Magnetic Resonance Research Center (UMRAM) **Esra Abacı**, **Emre Kopanoğlu**, **Burak Akın**, **Volkan Açıkel**, **Taner Demir** and **Haldun Özgür Bayındır** for their friendship and all the scientific collaborations that we made.

I want to thank **Erdem Ulusoy** for his "muhabbet" along all the "rakı" that we consumed. I also want to thank him for his musical companionship during the Tunali Hilmi Recitals.

I want to thank **Kıvanç Köse** for reminding me that there are many important aspects of life other than research.

I also want to thank my love **Gözde Karagöz** who simply made me a happier person. Thanks for sharing the burden.

I thank my **family** who supported me whenever I needed them.

Finally I want to thank everyone who made Ankara actually a pleasant city to live. It was a true miracle.

Table of Contents

List of Figures:

observed with the minimum heating mode, the maximum heating linear mode and the quadrature mode, respectively.

List of Tables

1. INTRODUCTION

Magnetic Resonance Imaging (MRI) is a safe imaging technology that provides many clinical benefits. Basically, MRI is performed by exciting magnetic spins with radiofrequency (RF) pulses and receiving the response generated by these spins as they relax into their original state. This response is spatially encoded by using the gradient fields and converted to an actual image.

Although it is not desirable, the body is exposed to an electric field during the RF excitation of the spins. This electric field may cause heat dissipation as it penetrates the conductive medium of body tissues. The specific absorption rate (SAR) is used as a measure of the electromagnetic (EM) power dissipated in a given volume. Current regulations set limits [1] on both the average whole body SAR and the peak local SAR in order to ensure the safety of patients. Furthermore, regulations limiting the maximum temperature increase in different parts of the body are also included.

The average-volume SAR is a factor that limits the maximum power that can be used for the RF excitation. The reduction of the average SAR is important for two reasons. First, an approximately quadratic relationship exists between the SAR and the operating frequency of the MRI. The frequency in MR scanners has increased over the years in order to benefit from the SNR advantages obtained at higher field strengths. Because SAR limits have remained the same, SAR reduction techniques must be developed in order to ensure patient safety in the higher field strengths. Second, the average SAR increases as the duration of the RF pulse decreases. Therefore, if fast scans with short RF pulses are to be implemented, the SAR should be reduced.

The SAR may depend on both the transmit coil design and the sequence parameters. Accordingly, there are approaches that focus on tailoring the RF excitation and redesigning the MR sequences in order to reduce the average SAR [2-4]; other methods are based on designing new transmit coil geometries and RF shimming [5]. Methods that adopt both of these approaches for SAR

reduction have also been investigated [6]. Transmit arrays are promising due to the freedom of exciting the spins with multiple elements simultaneously [7]. With that freedom, the SAR problem can be solved, along with the problem of RF field inhomogeneity. In most of the applications, a spatially homogenous RF excitation is usually desirable in order to obtain high-quality MR images. The RF field homogeneity is especially reduced in higher field strengths where the wavelength is comparable to the body size. RF shimming [8] and transmit sense [6] methods can be used with transmit arrays to solve the homogeneity problem while handling the SAR problem simultaneously.

In the presence of metallic devices, the local SAR becomes more important for safety. The current clinical MR scanners operate safely within the SAR limits. However, when metallic devices are present in the patient, the SAR amplification near the device can be dangerous [9-12]. When the local SAR is amplified, the temperature may increase excessively in the vicinity of the device, and tissue damage and burns may occur [13]. To prevent this, patients carrying metallic devices are not allowed into the MR scanner; considering that there are many people in the world who have metallic implants, the importance of this problem can be appreciated. There is also a risk related to local heating around metallic devices in interventional procedures. With the advent of interventional MRI, it is now possible to perform catheterization and biopsy procedures under MRI guidance; however, RF safety problems introduce additional risks with these procedures [14-17]. A solution that directly addresses this safety problem may increase the quality of life of millions of people.

In general, for both diagnostic and interventional procedures, the reduction of RF heating of metallic devices is crucial for patient safety. Many solutions to this problem have been proposed in the literature. In most of these works, the device or its long conductor extension is modified electrically in order to prevent heating [18-21]. Although this approach is promising, in some applications, such as MR-guided biopsy procedures [22], it may be impractical to make a modification to the device. Furthermore, in the case of implanted devices, such as pacemakers and deep brain stimulators (DBS), the replacement

of the device with a safer one may not always be convenient for patients. Thus, instead of modifying the device, the electromagnetic (EM) field surrounding the device can be modified to reduce the RF heating, such that replacing the metallic device with a safer version is no longer necessary.

The modification to the electric field should be made in order to reduce the RF heating only, and the resulting MR image quality should not be affected. In this thesis, methods to achieve this task are investigated. By modification of the EM field distribution, the RF heating of the human body was shown to be reduced. In Chapter 2, this approach is demonstrated to minimize the average SAR while keeping the magnitude of the transmit sensitivity unchanged. In addition, it is shown that, by releasing the phase constraint of the transmit sensitivity, the average SAR can be reduced even further. The optimum field solution that results in the minimum average SAR was also calculated [23].

Different RF excitation methods are used to reduce the RF heating due to implanted devices in the third chapter of the thesis. Evidence is provided that, a linearly polarized coil can be used to safely scan a patient with an implant [24]. The zero electric-field plane of the coil was coincided with the implant in order to prevent the tip heating of the metallic device. Furthermore, the transmit sensitivity characteristics of the coil were preserved with respect to a quadrature coil. This approach required either rotating the coil or the patient in order to reduce the electric field in the vicinity of the device. In Chapters 4 and 5, a similar task was achieved by using a two-channel and a multi-channel transmit array [25, 26], where the patient or the coil remained constant and the EM field was altered. In Chapter 4, a method to monitor the induced current on a metallic device is also presented. The method was based on measuring the induced current artifacts in the MR images: the safest two-channel excitation that cancelled the current on the device was found, and the RF heating was minimized. The application of a similar method to the multi-channel excitation is discussed in Chapter 5, with the average SAR and homogeneity issues also being addressed. Lastly, in Chapter 6, the effect of the phase variation of the electric field on the heating of the metallic device is investigated [27]. It is

shown that a linear-phased electric field variation would amplify the heating at one of the tips of a metallic wire and reduce the heating at the other one. The lead/wire geometry was modified in order to achieve such a condition. Additionally, a similar idea was tested with transmit arrays, which were used to generate an electric field whose phase changed linearly along the lead. A demonstration of the tip SAR amplification and reduction is provided.

2. MINIMUM SAR FOR RF SHIMMING BY ALLOWING SPATIAL PHASE VARIATION

2.1 Preface

The content of this chapter was presented (in part) in a conference publication [23], reference: Eryaman Y, Tunç C A., Atalar E "Minimum SAR for RF Shimming By Allowing Spatial Phase Variation" Proc Intl Soc Mag Reson Med 18(2009):4777.

2.2 Introduction

The Specific Absorption Rate (SAR) is a patient safety parameter that should be seriously considered in MRI procedures. There are many studies in the literature in which the whole body average SAR has been minimized under conditions of satisfying a target transmit sensitivity [5,6]. In one of these studies, the SAR due to a given multi-channel transmit coil was minimized with respect to the phase and the magnitude of the excitation currents of the individual channels [5]. In another work, the ultimate value of the SAR for transmit sense was calculated by the optimization of the field inside a homogenous body model [6]. In these studies, the target transmit sensitivities were chosen in order to obtain a uniform magnitude field distribution. However, reducing the SAR by relaxing the phase constraints of the target profile was not investigated. In the study presented here, by keeping the magnitude distribution of the target transmit profile within a given boundary, the phase distribution was optimized to obtain the true ultimate SAR for the MRI coils. It was shown that it was possible to reduce the whole body SAR by orders of magnitude up to 30, while realizing a desired magnitude distribution for target sensitivity. For this purpose, the related optimization problem was solved by Particle Swarm Optimization (PSO) [3]. PSO is a search algorithm that can easily be implemented and used to solve optimization problems with various constraints. By using PSO, the optimum EM field distribution that satisfied the above conditions was calculated. Using well-known techniques [6], the current distributions that can generate the optimum field inside the

body model can also be calculated. These optimum current paths can be used to optimize RF coils and to obtain a minimum whole body SAR.

2.3 Theory

The average whole body SAR for a homogenous body model depends on the volume integral of the magnitude square of the electric field distribution, as shown below:

$$SAR = \sigma / M \int_{body} |E|^2 \, dv \qquad (1)$$

In this expression, σ is the conductivity, and M is the total body mass.

During MRI, it is usually desirable to obtain a uniform transmit sensitivity profile. In order to achieve that, the forward polarized field component, H_f, should be constrained on desired locations in the body. For any given point of interest (ρ_0, ϕ_0), the expression for the H_f in cylindrical coordinates is shown below:

$$H_f = (H_\rho - jH_\phi)e^{-j\phi} \qquad (2)$$

where H_ρ and H_ϕ are the magnetic field components in the radial and angular directions, respectively.

In order to make a general formulation for the problem, the cylindrical basis expansion can be formulated to express the field, as follows:

$$\vec{E} = \sum_{m=-\infty}^{\infty} \sum_{n=-\infty}^{\infty} \vec{E}_{mn} \qquad (3)$$

The expression for each separate mode, $\vec{E}_{mn}$, can be written as $\vec{E}_{mn} = E_{mn} \cdot \vec{\alpha}_{mn} \cdot e^{jm\phi} e^{-j\beta_z z}$, where ϕ and z are the angular and z coordinates in the cylindrical coordinate system, respectively, and m and n are integer variables representing the expansion modes. E_{mn} is a 3x2 matrix and is a function of ρ, the radial coordinate, but not ϕ or z, and $\vec{\alpha}_{mn}$ is a

2x1 vector whose elements are the constants that multiply the basis functions and $\vec{\alpha}_{mn} = [A_{mn} B_{mn}]^{T}$.

The E_{mn} matrix and its components are shown below:

$$E_{mn} = \begin{bmatrix} J_m(\beta_{\rho n}\rho) & 0 \\ \dfrac{1}{\rho\beta} J_m(\beta_{\rho n}\rho) & \dfrac{\omega\mu}{\beta} J'_m(\beta_{\rho n}\rho) \\ -jJ'_m(\beta_{\rho n}\rho) & \dfrac{1}{\sigma'\rho} J_m(\beta_{\rho n}\rho) \end{bmatrix} \tag{4}$$

Using the basis expansion, the forward polarized field component, H_f, can also be expressed, as follows:

$$H_f(\vec{r}) = \sum_{mn} H_{fmn}(\vec{r}) \cdot \vec{\alpha}_{mn} \tag{4}$$

where each separate mode for H_f can be expressed as shown below:

$$H_{fmn}(\vec{r}) = \left[\frac{j\sigma'}{\sqrt{2}\beta_\rho}, \frac{\beta_z}{\sqrt{2}\beta_\rho} \right] J_{m+1}(\beta\rho) e^{j(m+1)\phi} \tag{5}$$

Here, σ' denotes the complex conductivity of the medium. β_{zn} and $\beta_{\rho n}$ are the wave numbers along the longitudinal and radial directions, respectively, which can be calculated as $\beta^2 = -j\omega\mu_0[\sigma + j\omega_0\varepsilon]$, where L is the length of the cylinder.

For the case where the number of points of interest is equal to k, the whole constraint on the values of H_f can be written in the following matrix form:

$$B\alpha = c \tag{6}$$

where *c*, the desired transmit sensitivity profile, is represented by a kx1 vector whose elements are equal to the desired H_f values at each point of interest. α is a column vector that contains the weighting coefficients (A_{mn} and B_{mn}) for each separate mode. Lastly, *B* is the transmit sensitivity matrix whose elements are equal to the basis functions of H_f evaluated at the desired point of interests.

The average whole body SAR in the homogenous body model can be written as follows:

$$SAR = (\sigma / M) \times \sum_{mn} \vec{\alpha}_{mn}^{\;H} \cdot R_{mn} \cdot \vec{\alpha}_{mn} \tag{7}$$

where R_{mn} is a Hermitian matrix and can be computed by using the following expression [6]:

$$R_{mn} = \left[2\pi L\sigma \int_0^{r_{body}} E_{mn}^{\;H} \cdot E_{mn}\rho d\rho \right] \tag{8}$$

The average whole body SAR can be expressed in a shorter form, as $\alpha^* R\alpha$, where R is the electric field cross-correlation matrix whose block diagonals are equal to R_{mn}.

After the definition of required variables, the SAR minimization problem can then be expressed as follows:

$$\min \quad \alpha^* R\alpha \quad \cdot \tag{9}$$
$$B\alpha = c$$

The solution for this problem can easily be found by using the Lagrange optimizer method, as shown below:

$$SAR_{avg} = c^* (BR^{-1}B^*)^{-1} c \tag{10}$$

In MRI, the magnitude distribution of the transmit field profile is usually desired to be homogenous. However, the phase distribution is a free parameter that can be optimized in

order to obtain a minimum whole body SAR. If the S matrix is defined as $S = (BR^{-1}B^*)^{-1}$, then the minimization problem above can be expressed as follows:

$$\min \quad c^* S c \tag{11}$$
$$1 - \delta < |c_i| < 1 + \delta \quad for \quad i = 1, 2, \ldots k$$

where k is the number of sample points in the target transmit field profile, and δ is the tolerance for the magnitude of H_f.

As will be shown later, the solution of this problem will significantly decrease the SAR while preserving the magnitude distribution of the transmit sensitivity.

2.4 Simulations

In all solutions, a homogenous body model diameter of 0.2 meters and a length of 1 meter were assumed (Figure 2.1).

D= 0.2 m   L=1 m
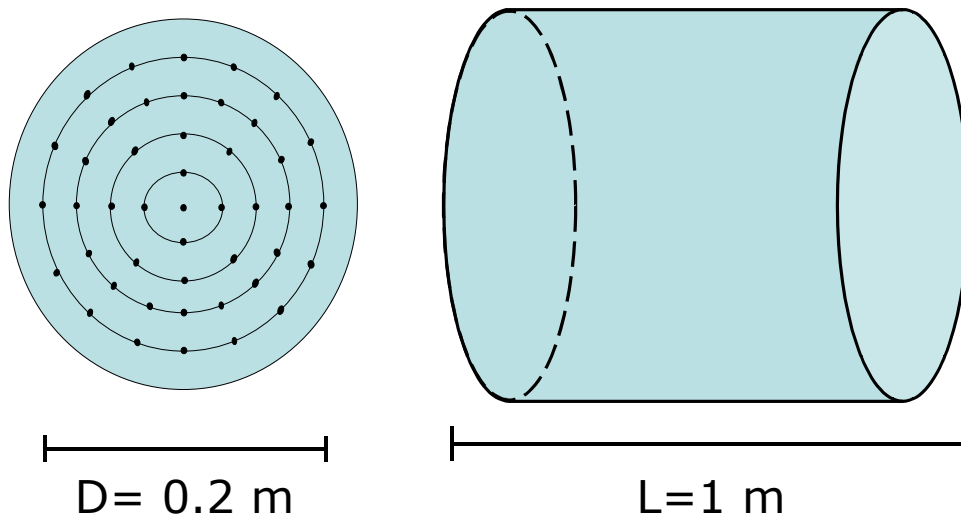
Figure 2.1 The homogenous body phantom model with uniform electromagnetic properties is shown. The target transmit profile is obtained by constraining the field at 45 sample points, which forms a circular region of radius 8 cm.

The relative permeability and permittivity for the phantom were chosen as 1 and 70, respectively. The conductivity was assumed to change linearly with the frequency, and it was taken as 0.4, 0.8 and 1.2 S/m for 1.5 T, 3.0 T and 4.7 T, respectively.

As an initial solution, the target profile was assumed to include only a single point of interest. This point was chosen as the center of the cylinder. For a single-point profile, varying the phase of H_f for that point of interest did not have an effect on the minimum whole body SAR. The optimum coil sensitivity and the minimum whole SAR were calculated for 1.5 T, 3.0 T and 4.7 T.

To obtain a homogenous transmit sensitivity, multiple numbers of points were used for the target profile. First, a zero phase profile was assumed, and the corresponding optimum sensitivity and minimum SAR were calculated. Then, in order to generate the optimum phase distribution, the PSO algorithm [3] was used to solve the problem. A MATLAB (version 7.0, MathWorks Inc., Natick, MA) program was written to implement the algorithm. For the target transmit field profile, H_f was constrained to have a uniform magnitude at 45 sample points, which formed a circular region of a radius of 8 cm. Figure 2.1 shows the location of sample points that H_f constrained. The phase distribution is optimized by using the particle swarm optimization method in order to minimize the whole body SAR. The simulations were made for 3 field strengths, 1.5 T, 3.0 T and 4.7 T, and for 3 different tolerance values, $\delta = 0$, $\delta = 0.03$ and $\delta = 0.1$. Note that the transmit sensitivity was permitted to fluctuate in the interval $[1-\delta, 1+\delta]$. The SAR reduction with respect to a zero phase transmit profile was calculated. The optimum H_f distribution was calculated for the $\delta = 0$ case at 3 field strengths. Electric field maps related to the zero phase and optimum phase solutions were also generated.

2.5 Results

For the PSO solutions, the number of particles, the constriction factor and the cognitive and social rates for velocity updates were chosen, as explained in a previous work [40]. The fitness function was defined as the ratio of the average SAR. Each simulation lasted

for 50-100 seconds using a PC with an AMD Athlon™ 64 Processor and 2.41 GHz 4 GB RAM.

As an initial solution, the target profile was assumed to include only a single point of interest. This point was chosen as the center of the cylinder and sets a lower bound for all of the other solutions. As will be shown, larger profiles consisting of multiple locations will result in larger SARs when compared with the solution found by using a single point of interest. Figure 2.2 shows the sensitivity variation in the z=0 transverse plane at 3 field strengths. Because SAR will depend on sequence parameters, such as flip angle and TR, the SAR value for each solution is reported here in arbitrary units.

(1.5 T)   (3.0 T)

(4.7 T)
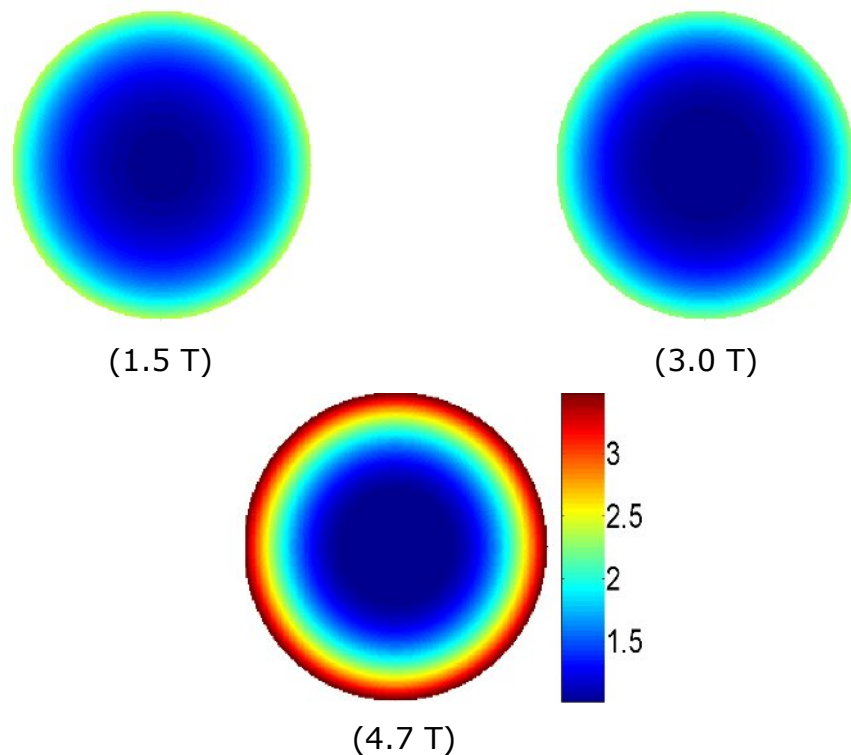
Figure 2.2 The optimum transmit sensitivity for imaging a single point of interest is shown. Because the target profile consists of a single point, the sensitivity profile solutions are not homogenous.

The SAR values obtained by each solution were 1, 6.51 and 29.66 arbitrary units (au). For these solutions, the relationship between the average SAR and field strength was

expected to be quadratic. However, it was also assumed that the conductivity increased with the field strength. Therefore, the increase in the SAR due to the field strength was larger than a quadratic increase.

As the second solution, a uniform magnitude target profile was assumed; the phase of the target profile was assumed to be constant as well. The sensitivity of the optimum solution is shown in Figure 2.3.
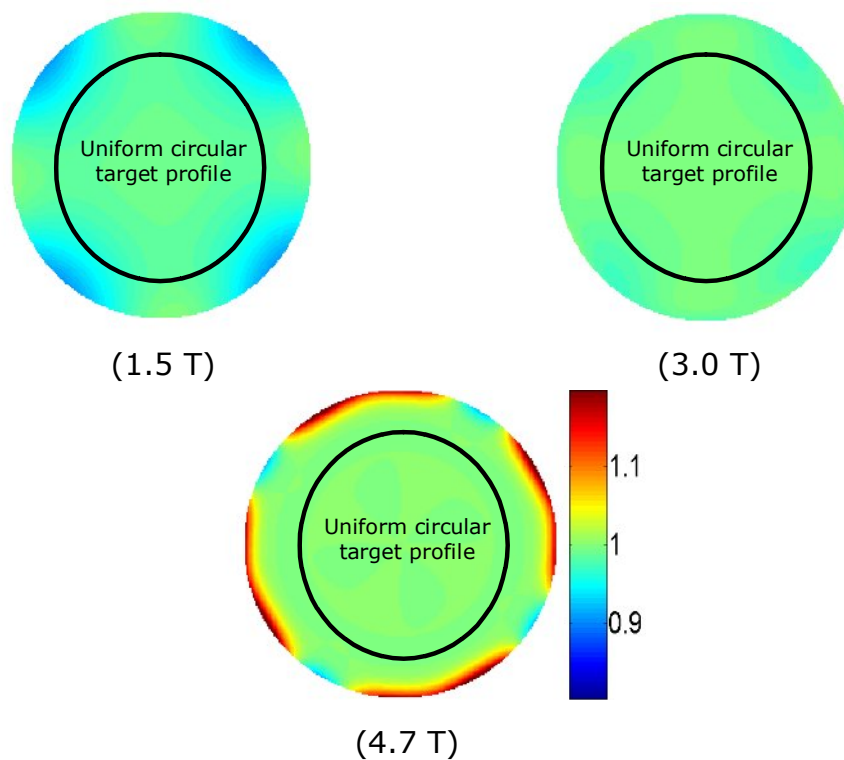
Figure 2.3 The optimum transmit sensitivity for imaging a target profile is shown. Because the target profile consists of multiple points, the sensitivity solutions are homogenous. The phase throughout the profile was assumed to be constant.

As expected, an almost perfectly homogenous sensitivity solution was obtained in the transverse plane for all of the field strengths. However, this homogeneity resulted in an increase in the average SAR. The SAR values obtained for these solutions were 4.30**,** 452 and 53,287 au for 1.5 T, 3.0 T and 4.7 T, respectively. This increase can easily be

explained by the modal expansion of the EM field inside the phantom model. The modal expansion of a uniform profile in the space requires using modes with large indices. These modes exhibit a fast spatial variation in both the angular and longitudinal directions. Therefore, their SAR contribution to the solution is significantly higher than the modes with slower spatial variation. Therefore, an increase in SAR due to a homogenous target profile constraint is physically unavoidable. It should also be noted that among the infinitely many solutions satisfying the uniform phase-constant magnitude sensitivity profiles, these solutions have the minimum average SAR.

However, to alleviate this SAR problem, a different approach can be implemented. Although it is desirable to obtain a uniform magnitude distribution, the phase variation of the sensitivity is not a constraint. For this purpose, the optimization problem mentioned in Equation 11 is solved. The resulting transverse sensitivity solutions are shown in Figure 2.4.

(1.5 T)   (3.0 T)

(4.7 T)
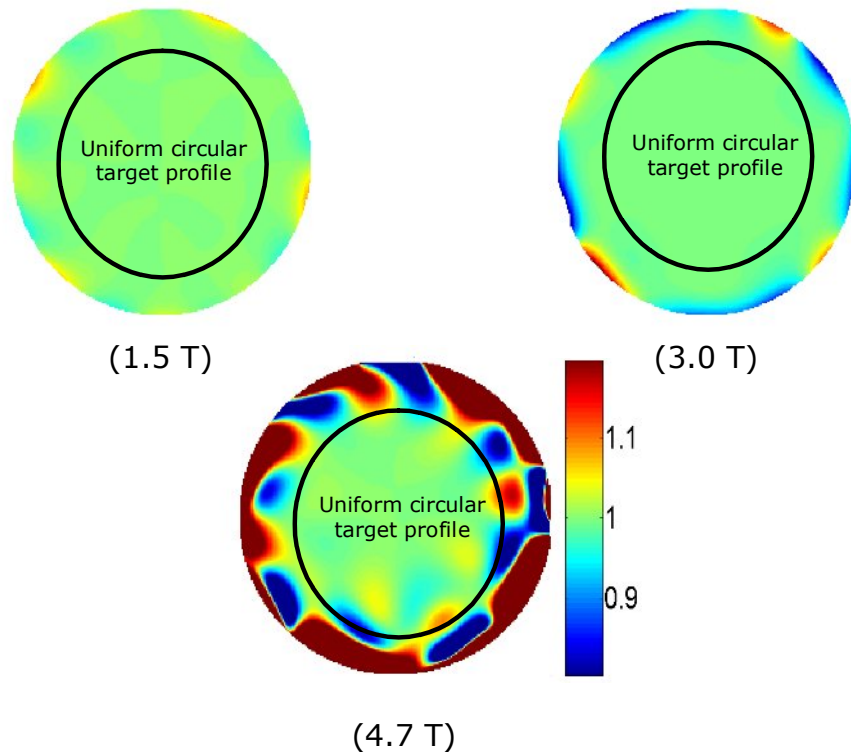
Figure 2.4 The optimum transmit sensitivity for imaging a target profile is shown. Because the target profile consists of multiple points, the sensitivity solutions are homogenous. The phase throughout the profile is also optimized to minimize the average SAR.

Similar to the previous solution, the magnitude variation was kept constant through the target profile. The phase variation, however, was optimized to minimize the average SAR. Figure 2.5 shows the magnitude and the phase of the transmit sensitivity sampled in the radial direction.
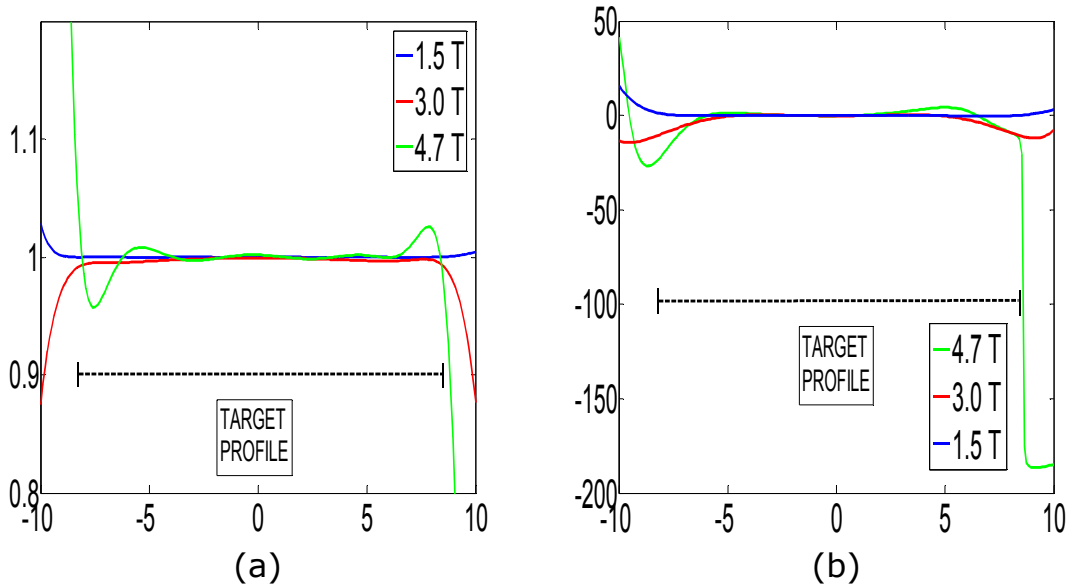
Figure 2.5 The transmit sensitivity due to the optimum solution sampled in the radial direction. The transmit sensitivity profile is homogenous in magnitude, as seen in Panel a. The phase variation is tolerated in order to minimize the average SAR, as seen in Panel b.

The SAR due to the optimum solutions was 1.64, 77.3 and 4027 au for 1.5 T, 3.0 T and 4.7 T, respectively. Clearly, by releasing the phase constraints, a reduction with respect to the uniform phase solution was achieved. Similarly, by releasing the magnitude constraint, a reduction in SAR can be realized. For this purpose, the magnitude of the field was permitted to fluctuate in the interval $[1-\delta, 1+\delta]$, as indicated in equation 11. Three different ∂ values, 0, 0.03 and 0.1, were used for the solutions. Table 1 shows the

amount of the reduction in the SAR with respect to the uniform magnitude-uniform phase solution.

SAR REDUCTION	$\delta=0$	$\delta=0.03$	$\delta=0.1$
1.5 T	2.62	2.67	2.67
3.0 T	5.86	10.97	12.66
4.7 T	12.95	35.06	37.8

Table 1 Reduction in the SAR with respect to the uniform magnitude-uniform phase solution is shown.

As expected, as the constraints are released, the number of freedoms increases, and the SAR can be reduced further. Note that a maximum reduction of 37.8 was obtained with $\partial=0.1$. With this solution magnitude, the sensitivity was permitted to fluctuate between 0.9 and 1.1.

It should be noted that the field solutions are also critical to understand and design better RF coils with less average SAR. For this purpose, electric field variation should also be investigated. The z component of the electric field of both the uniform phase solutions and the optimum solutions were calculated for 1.5 T, 3.0 T and 4.7 T and are shown in Figure 2.6, Figure 2.7 and Figure 2.8, respectively. $\partial=0$ is assumed for all of the solutions. The longitudinal component of the field can be used to identify the coil geometry and the current paths on the coil.

(a)   (b)
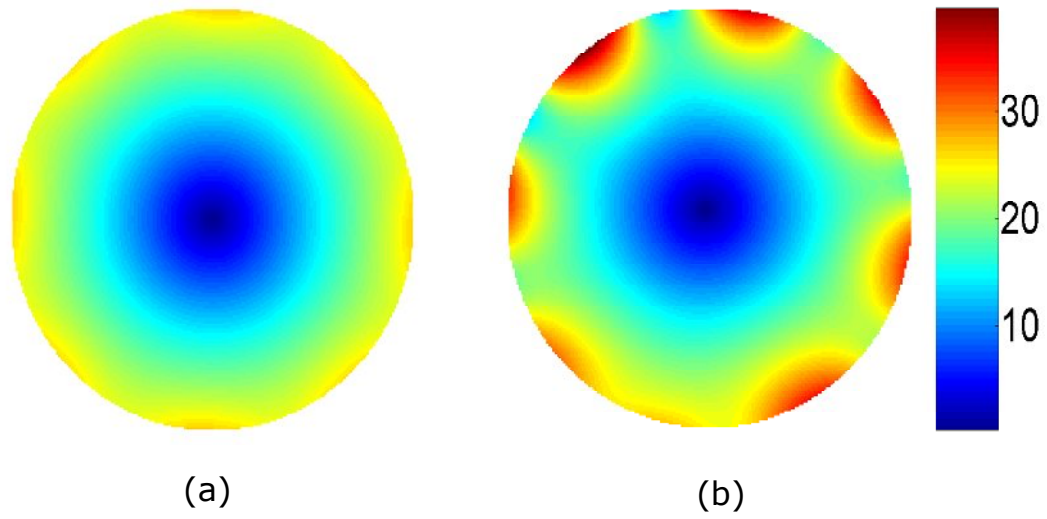
Figure 2.6 The z component of the electric field in the z=0 transverse plane (1.5 T). The uniform phase solution is shown in Panel a, and the optimum solution is shown in Panel b.

(a)   (b)
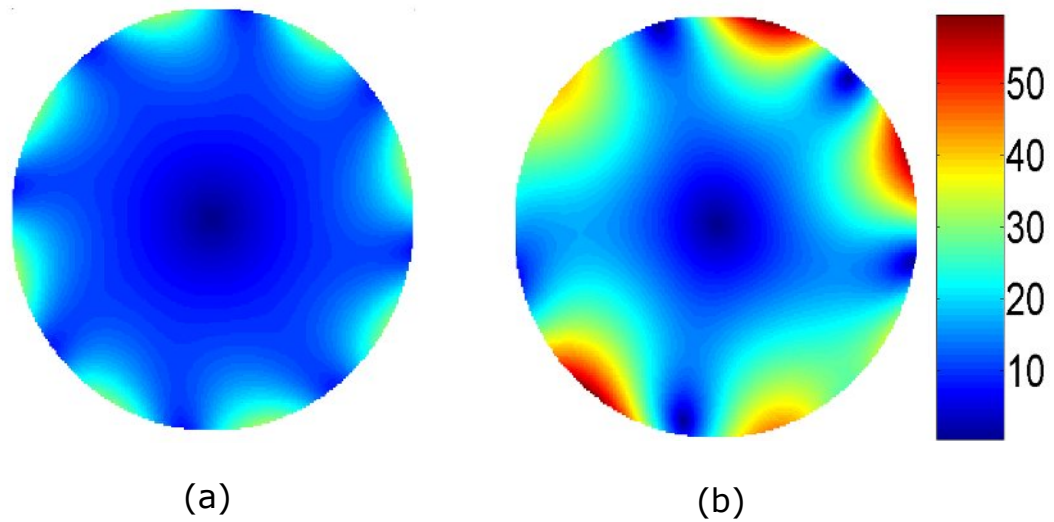
Figure 2.7 The z component of the electric field in the z=0 transverse plane (3.0 T). The uniform phase solution is shown in Panel a, and the optimum solution is shown in Panel b.

(a)   (b)
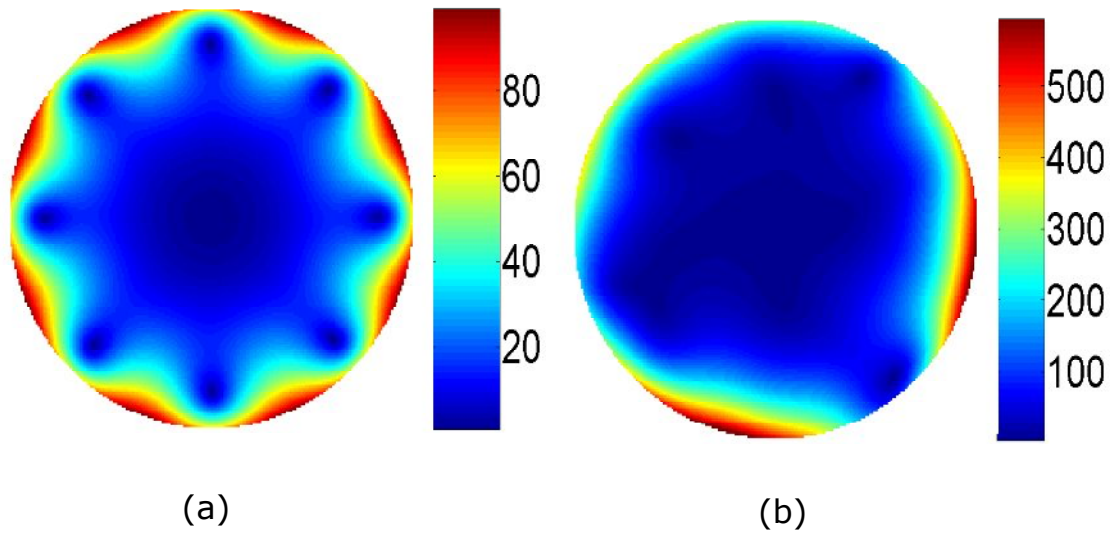
Figure 2.8 The z component of the electric field in the z=0 transverse plane (4.7 T). The uniform phase solution is shown in Panel a, and the optimum solution is shown in Panel b.

In order to understand the geometry of the RF coil, the longitudinal variation of the electric field should also be investigated. Figure 2.9, Figure 2.10 and Figure 2.11 show this variation for both the uniform phase and optimum solutions.

(a)   (b)
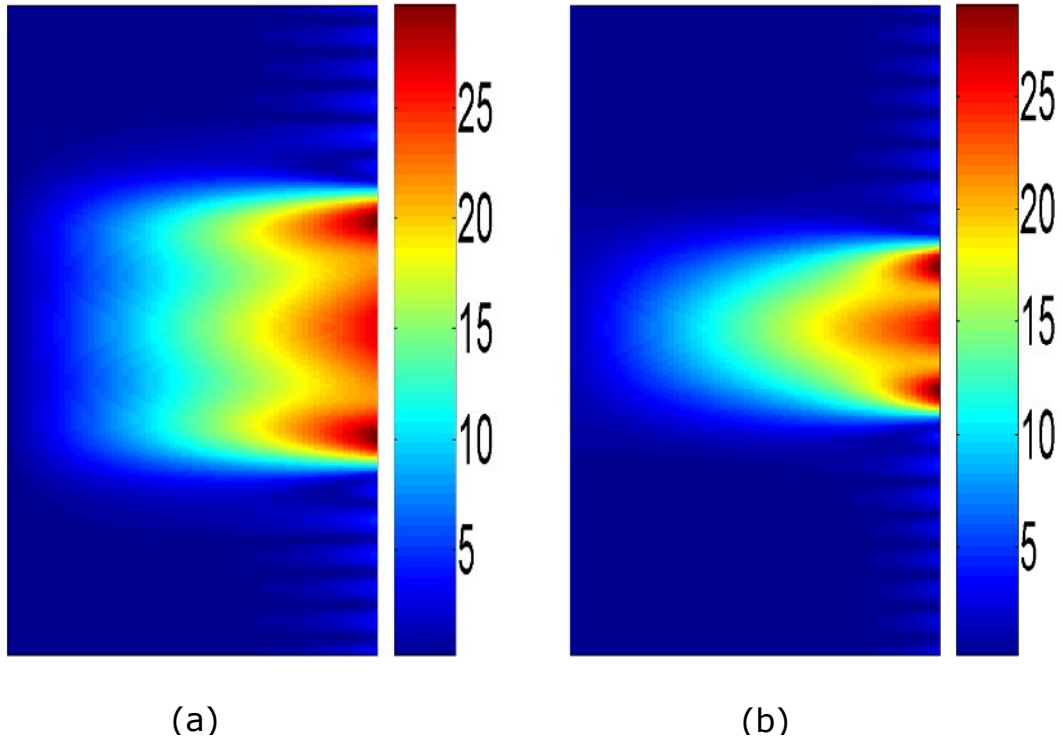
Figure 2.9 The z component of the electric field in the $\phi = 0$ half plane (1.5 T). The uniform phase solution is shown in Panel a, and the optimum solution is shown in Panel b.

(a)   (b)
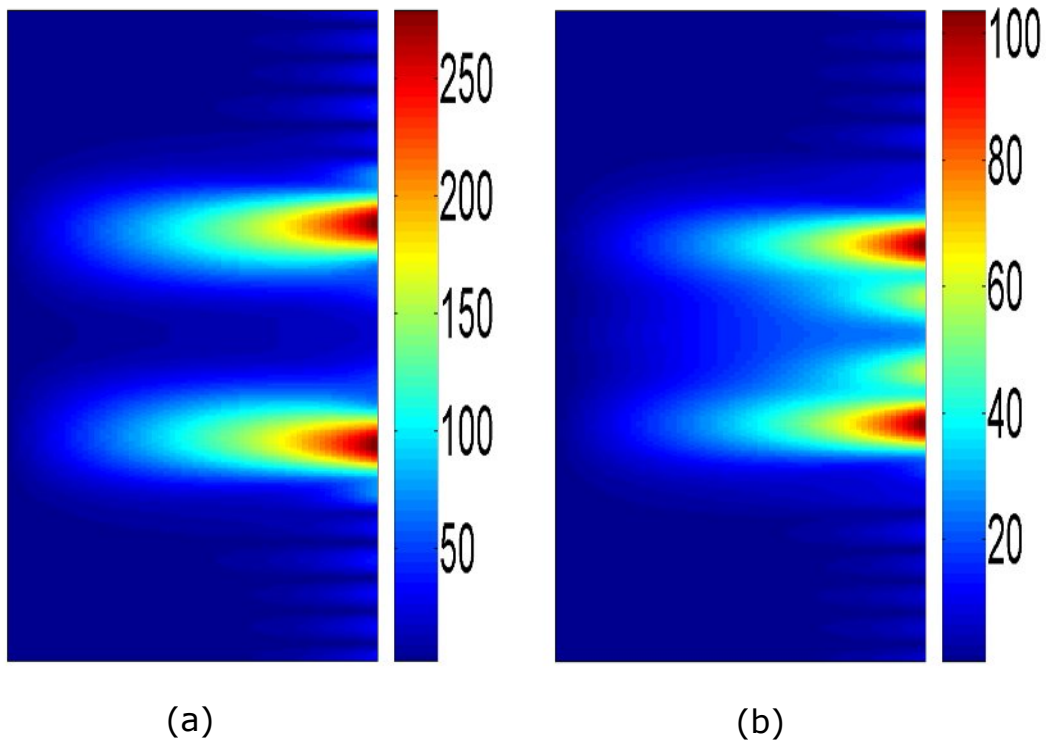
Figure 2.10 The z component of the electric field in the $\phi = 0$ half plane (3.0 T). The uniform phase solution is shown in Panel a, and the optimum solution is shown in Panel b.

(a)   (b)
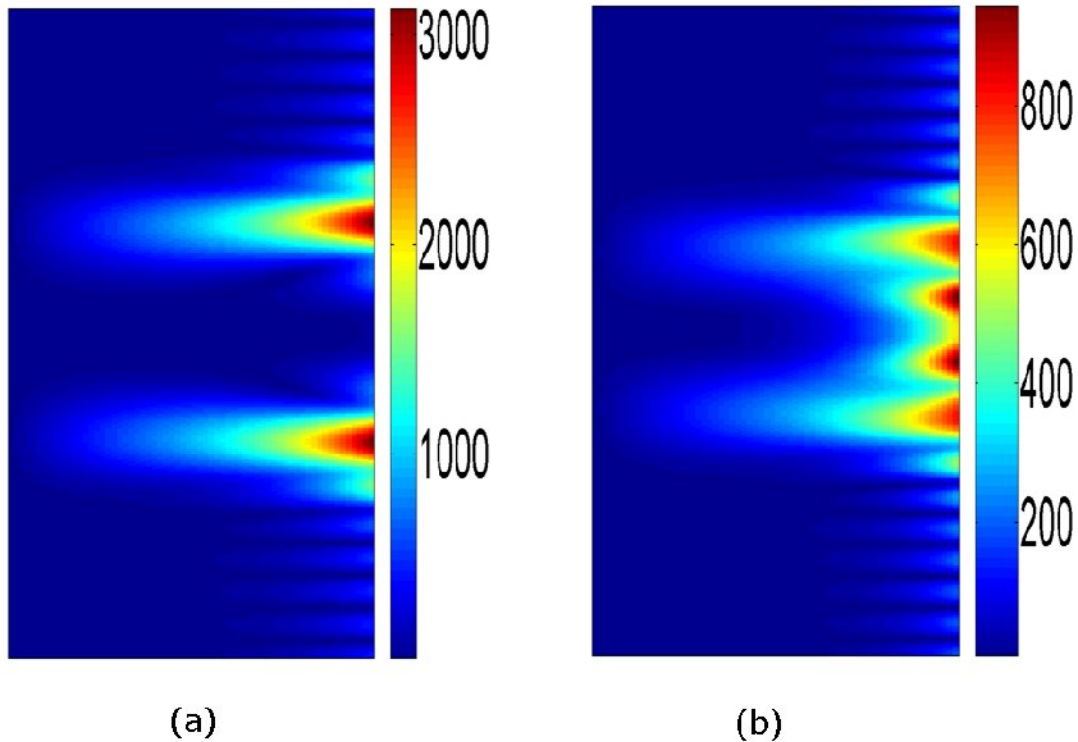
Figure 2.11 The z component of the electric field in the $\phi = 0$ half plane (4.7 T). The uniform phase solution is shown in Panel a, and the optimum solution is shown in Panel b. $\partial = 0$ is assumed.

2.6 Discussion

From Figure 2.5, Figure 2.6 and Figure 2.7, it can be seen that transmit arrays can be used to realize field variations. The electric field due to each channel element is visible in Figure 2.5. The number of channels can be identified by a visual inspection of the results. Because the field varies in the angular direction, the coil elements can be fed with the appropriate excitation currents to approximate these field solutions.

Furthermore, it can be seen from Figure 2.9, Figure 2.10 and Figure 2.11 that the electric field has a variation in the longitudinal direction. This may be achieved by modulating the amplitude of the conductor currents or the geometry of the coil in a longitudinal direction, such that the optimum field is approximated. Transmit array elements can be placed in a longitudinal direction with the same motivation as well. In all cases, the

solutions show that the effective length of the coil varies from one-third to one-half of the body length for different field strengths.

2.7 Conclusion

In this work, the minimum average whole body SAR for RF shimming was calculated. The EM field of a transmit coil was optimized in order to achieve a homogenous transmit sensitivity and minimum whole body SAR. The reduction in SAR due to relaxing the phase and magnitude constraints was calculated. The optimum coil sensitivities and electric field magnitude distributions are also presented.

3. REDUCTION OF IMPLANT RF HEATING THROUGH MODIFICATION OF TRANSMIT COIL ELECTRIC FIELD

3.1 Preface

The content of this chapter was published in a journal paper[24] Reference: Eryaman, Y., Akin, B. and Atalar, E. Reduction of implant RF heating through modification of transmit coil electric field. Magnetic Resonance in Medicine, n/a. doi: 10.1002/mrm.22724))

3.2 Introduction

Magnetic resonance imaging (MRI) is known as a very safe imaging technology. However, because of the possibility of inducing excessive currents on the metallic wires, MRI scanning is generally not performed on people with metallic implants such as pacemakers. A radio-frequency (RF) electric field, although undesirable, is often generated in the body during the excitation of spins with RF magnetic field pulses. Power absorbed by the body under this electric field is determined by the specific absorption rate (SAR) and needs to be kept at a level that is safe to the patients. If a patient with a metallic implant is examined using MRI, a very significant SAR amplification may occur around the implant, which may cause excessive body heating and burns. Due to this well-known problem, patients with metallic implants are currently not allowed inside the MRI scanners.

Previous studies [9,10] have assessed the implant heating problem via both in vitro and in vivo approaches. Mathematical models have also been presented [11,12] and the validity of these models has been further verified by comparison with the experimental data. A detailed analysis of the problem was conducted in [11] by solving the bio-heat equation with Green's function and the linear

system theory. The maximum steady-state temperature increase in the tissue near a transmitter catheter antenna was calculated. In [12], a parameter called the "safety index" was introduced, which combines the effect of the SAR gain of the implant lead and the bio-heat transfer process to measure the in vivo temperature changes. Variations of the safety index with respect to the length and radius of the implant lead, the thickness of the insulation, tissue conductivity and permittivity were also investigated. These studies presented a good model of tissue heating caused by metallic wires in RF fields. In another study, experimental methods were developed to measure and monitor the RF-induced currents inside implants [29].

Modifications of the implant leads and wires for reducing the RF-induced heating were investigated in other studies. In two of these studies, a series of chokes was added to the coaxial cables [18,19] to reduce the currents generated on the cable shield. In another study [20], the effects of coiled wires on induced heating were investigated. By introducing air gaps and lowering the parasitic capacitance, the self-resonance frequency of a coiled wire was shifted to the operating frequency. This change increased the impedance of the wire and thus reduced the RF heating. However, all of these designs are based on modifying the lead wires or cables, which makes it difficult to produce mechanically robust leads. In addition, for patients who already have pacemakers, replacing the original leads with these modified safer leads may not always be feasible. For these reasons, modifications of the implant lead designs or the catheters may not always be the most appropriate solution for the MRI-induced RF heating of metallic wires.

The relationship between the electric field distribution and the temperature increase of the implant leads was recently investigated [30]. It was found that tissue heating depends on the orientation of the lead with respect to the direction of the electric field. To identify the worst-case scenario, an optimization-based approach was used in [31] to calculate the EM field that could produce the maximum heating at the wire tip. However, studies to optimize the EM transmitter field to minimize the implant heating were not carried out.

In this study, we showed that the transmitter coil field used in MRI could be optimized to steer the electric field away from the implant lead and thus prevent heating. As demonstrated experimentally, a linearly polarized birdcage coil could be used for this purpose. Although this approach preserved the homogeneous transmit sensitivity characteristics of the coil, it caused a doubling of the whole-body SAR. To alleviate this problem and achieve uniform sensitivity, we further modified the field of the transmitter coil to minimize both whole-body SAR and the implant heating. Details of this approach are described in the following sections.

3.3 Theory

3.3.1) Implant-Friendly RF Coil

In the standard quadrature birdcage coils, the electric field is uniform in the angular direction but varies roughly linearly in the radial direction [32]. Therefore, an implant lead placed at the edge of the body experiences a high electric field, which induces currents both on the lead and in the body and eventually causes local SAR amplification. The electric field distribution of a standard forward polarized quadrature birdcage coil in an infinitely long homogeneous model can be approximated by ignoring the end-ring currents as follows (see the appendix for a detailed derivation):

$$E_z = \frac{-H_f \omega \mu_0 \rho}{2} e^{j\phi}, E_\phi = 0, E_\rho = 0 \qquad (12)$$

where E_z, E_ϕ, E_ρ are the longitudinal, angular and radial components of the electric field, respectively; H_f is the transmit sensitivity of the coil; ω is the Larmor frequency; μ_0 and ε are the permeability and permittivity, respectively; σ is the conductivity of the homogeneous model; ρ and ϕ are the radial and angular coordinates in the cylindrical coordinate system, respectively; and j is the imaginary number defined by $\sqrt{-1}$. Similarly, the electrical field of a linearly polarized coil can be expressed as follows:

$$E_z = -H_f j\omega\mu_0\rho\sin\phi, E_\phi = 0, E_\rho = 0 \qquad (13)$$

Note that j indicates a 90-degree phase shift with respect to a real field expression. As can be seen from the above equations, linear and quadrature birdcage coils have similar transmit sensitivity yet different electric field distributions. The transmit sensitivities of each coil are approximately uniform in the transverse plane. (Please see the appendix for the detailed derivation.) It can be noted from the above equation that the electric field is zero over the entire $\phi = 0$ plane. This plane can be steered into any angular direction by either changing the feeding location or simply rotating the linear birdcage coil. The same task can also be performed by controlling the amplitudes of the currents fed into the two ports of a quadrature birdcage coil. For example, if port-1 and port-2 are set in such a way as to make the corresponding electric fields zero at the $\phi = 0$ and $\phi = \pi/2$ planes, respectively, then the excitation currents with relative amplitudes of $\cos\phi_0$ and $\sin\phi_0$ at ports 1 and 2 would generate a zero electric field plane at $\phi = \phi_0$. Note that $\phi = \phi_0$ plane covers both $\phi = \phi_0$ and $\phi = \phi_0 + \pi$ half planes. If an implant lead lies on the zero electric field plane, there will be no induced currents on the lead. Because setting the electric field to zero makes the perpendicular component of the magnetic field vanish at the same plane, this method also intrinsically prevents the H-field coupling.

Using a linear birdcage coil solves the heating problem for an arbitrarily shaped implant lead when the lead is located in the zero electric field plane. Despite this modification of the electric field distribution, the transmit sensitivity is not significantly disturbed. However, as previously shown [33], linear birdcage coils are not efficient for RF transmission when the volume average SAR is considered. For linear excitation, a reverse polarized field component co-exists with the forward polarized component, and the whole-volume average SAR per unit flip angle is doubled.

3.3.2) Transmit Field Optimization

To alleviate the doubling problem of the whole-volume average SAR, a general formulation was developed. Because transmit sensitivity is determined by the forward polarized component of the magnetic field and SAR is determined by the electric field distribution, the above-mentioned problem can be solved by optimizing the electromagnetic field of the coil [6]. In this study, we successfully demonstrated the feasibility of such a strategy by obtaining the desired electromagnetic field distribution in the body. Although the work is not trivial, once an optimum electromagnetic field is identified, it is possible to design a coil that produces the desired field. The design of such an optimum implant-friendly coil is left for a future study.

First, we assumed that the optimization would be conducted in a uniform cylindrical object. This assumption simplified the formulation but could also be used with the other geometries. Because a cylindrical object is assumed, the cylindrical basis functions were used to expand the optimum field solution that minimized the whole volume average SAR [34,35]:

$$\vec{E} = \sum_{m=-\infty}^{\infty} \sum_{n=-\infty}^{\infty} \boldsymbol{E_{mn}} \cdot \vec{\alpha}_{mn} \cdot e^{jm\phi} e^{-j\beta_z z} \tag{14}$$

where ϕ and z are the angular and z coordinates in the cylindrical coordinate system, respectively, and m and n respectively denote the index of the circumferential and longitudinal modes used in the basis expansion. $\boldsymbol{E_{mn}}$ is a 3x2 matrix that contains the electric field basis functions for the ρ, ϕ and z components as shown below:

$$\boldsymbol{E_{mn}} = \begin{bmatrix} J_m(\beta_{\rho n}\rho) & 0 \\ \dfrac{1}{\rho\beta} J_m(\beta_{\rho n}\rho) & \dfrac{\omega\mu}{\beta} J'_m(\beta_{\rho n}\rho) \\ -jJ'_m(\beta_{\rho n}\rho) & \dfrac{1}{\sigma'\rho} J_m(\beta_{\rho n}\rho) \end{bmatrix} \tag{15}$$

E_{mn} is a function of ρ, the radial coordinate, but not of ϕ or z. $\vec{\alpha}_{mn}$ is a 2x1 vector whose elements are the constants that multiply the basis functions and $\vec{\alpha}_{mn} = [A_{mn}B_{mn}]^T$.

The transmit coil sensitivity can be expressed by evaluating the forward polarized field, which can be written in the summation form as

$$H_f(\vec{r}) = \sum_{mn} \overline{H}_{fmn}(\vec{r}) \cdot \vec{\alpha}_{mn} \cdot e^{j(m+1)\phi} e^{-j\beta_{zn}z} \qquad (16)$$

Each separate mode for H_f can be expressed as follows:

$$\vec{H}_{fmn}(\vec{r}) = \frac{1}{\sqrt{2}}\left[\frac{j\sigma'}{\beta_{\rho n}}, \frac{\beta_{zn}}{\beta_{\rho n}} \right] J_{m+1}(\beta\rho) \qquad (17)$$

where $\beta_{zn} = \frac{2\pi}{L}n$, $\beta_{\rho n}^2 = \beta^2 - \beta_{zn}^2$ and $\sigma' = \sigma + j\omega\varepsilon$ [35]. Here, σ' denotes the complex conductivity of the medium, and β_{zn} and $\beta_{\rho n}$ are the wave numbers along the radial and longitudinal directions, respectively, which can be calculated as $\beta^2 = -j\omega\mu_0[\sigma + j\omega_0\varepsilon]$. L is the length of the cylinder.

For k points of interest, the whole summation in the H_f expression can be written in the following matrix form:

$$H\alpha = c \qquad (18)$$

where c, the desired transmit sensitivity profile, is represented by a kx1 vector whose elements are equal to the desired H_f values at each point of interest. α is a column vector that contains the weighting coefficients (A_{mn} B_{mn}) for each separate mode. H is the transmit sensitivity matrix whose elements are equal to the basis functions of H_f evaluated at the desired points of interest. H is a $k \times (2 \times M \times N)$ matrix, where M and N denote the total number of

circumferential (m) and longitudinal (n) modes that are used in the basis expansion. Implementing different field variations would require using different combinations of the cylindrical modes. To express a field exhibiting a rapid spatial change in the circumferential or the longitudinal direction, one must use higher-order modes in that particular direction. Therefore, to characterize an arbitrary EM field with this expansion, an infinite number of modes is required. For practical purposes, the number of modes is truncated in our study

The desired target transmit sensitivity is one of the linear constraints for minimizing the average SAR. A separate constraint also exists on the electric field to reduce the implant heating.

To achieve the zero-implant-heating condition, the components of the electric field that are parallel to the lead should be set to zero. Therefore, the induced current on the lead wire will be zero. This condition can also be expressed as a linear constraint, similar to H_f, as shown below:

$$E\alpha = \vec{0} \tag{19}$$

where $\vec{0}$ is a px1 vector with all of its elements equal to zero, and p denotes the number of sample points where the electric field is set to zero. E is a $k \times (2 \times M \times N)$ matrix, where M and N denote the total number of circumferential (m) and longitudinal (n) modes that are used in the basis expansion. E matrix contains the basis functions for E_z, E_ϕ and E_ρ evaluated at the desired zero electric field locations.

The constraints on H_f and the components of the electric field can be combined into a single matrix equation: $F\alpha = e$, where F and e are formed by concatenating the matrices B, E and the vectors c and $\vec{0}$, respectively.

While it is desirable to set the magnetic and electric field to certain values at points of interest, the specific absorption rate (SAR) needs to be under control. The expression for the average SAR is:

$$SAR = \sigma / M \int_{body} |E|^2 \, dv \tag{20}$$

where σ the conductivity, M is the total body mass and dv is the differential volume element . With the cylindrical mode expansion for a homogeneous body model, the resulting relation can be written as:

$$SAR = (\sigma / M) \times \sum_{mn} \vec{\alpha}_{mn}^{\;H} \cdot R_{mn} \cdot \vec{\alpha}_{mn} \tag{20}$$

where R_{mn} is a Hermitian matrix and can be computed using the following expression [35]:

$$R_{mn} = \left[2\pi L \sigma \int_0^r E_{mn}^{\;H} \cdot E_{mn} \rho \, d\rho \right] \tag{21}$$

where r denotes the radius of the homogeneous model. The average SAR can be expressed in a more compact form as $\alpha^* R \alpha$, where R is the electric field cross correlation matrix whose block diagonals are equal to R_{mn} .

Among the infinite number of solutions satisfying $F\alpha = e$, the solution with the minimum volume average SAR can be found by minimizing $\alpha^* R \alpha$. The solution for α can then be defined as:

$$\alpha_{opt} = R^{-1} F^* (F R^{-1} F^*)^{-1} e \tag{22}$$

The minimum whole body SAR value can be computed as:

$$SAR_{min} = e^* (F R^{-1} F^*)^{-1} e \tag{23}$$

These equations give the minimum possible SAR under the conditions of the desired transmit sensitivity and zero electric field near the implant. They also

give the corresponding weights for the cylindrical expansion modes. Although this solution does not directly specify the type of coil to be used, α_{opt} uniquely determines the EM field of the optimum coil. The significance of this result can be appreciated by experiments and simulations as explained in the next section.

3.4 Experiments and Simulations

3.4.1) Implant-Friendly RF Coil

To demonstrate the proposed theory, heating of metallic wires with both linear and quadrature excitation was tested. A phantom head model of 16 cm in diameter and 25 cm in length was prepared with commercially available gel (Dr Oetker Jello, Izmir, Turkey). To measure conductivity and relative permittivity, a cylindrical transmission line setup was used. By measuring the impedance at the end of the line and using the lossy transmission line impedance equations, the conductivity and relative permittivity were calculated [36]. A conductivity of 0.51 S/m and relative permittivity of 70 were obtained with 2.4 g/l of salt in the gel solution.

Heating experiments were performed with a straight wire and a curved wire, as shown in Figure 3.1. Both of the wires were tested with quadrature and linear excitation.
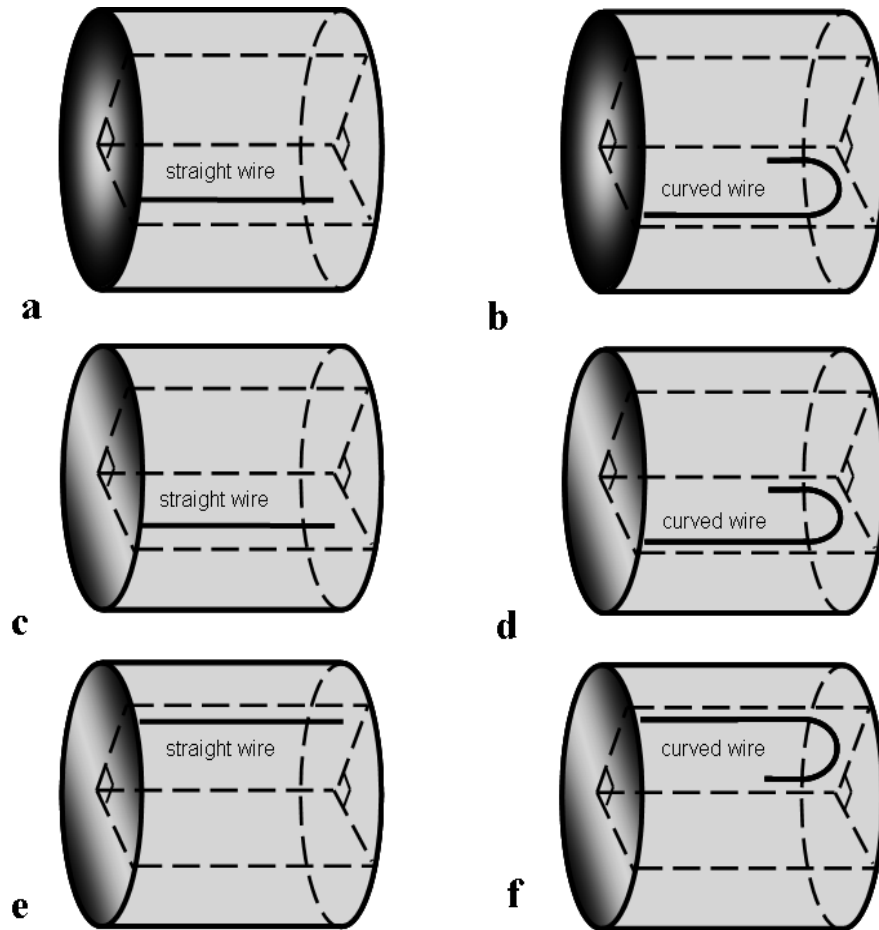
Figure 3.1 Gel phantoms with straight and curved wires. Fiber-optic temperature measurements were performed near the tips of the lead wires. (a) and (b), quadrature excitation; (c) and (d), linear excitation under the minimum heating condition; (e) and (f), linear excitation under the maximum heating condition.

The body coil of the Siemens 3.0 T Trio system was used in all experiments. A gradient echo sequence with a 4-msec TR and a 45-degree flip angle was used to scan the phantoms. A peak SAR value of 4.4 W/kg was obtained by finding the initial slope of the temperature rise and then multiplying it by the specific heat capacity of the gel, which was measured as 4100 J/kg/deg by using the KD2 Pro Thermal Properties Analyzer (Decagon Devices Inc, WA, USA). The temperature measurement was conducted at a depth of 1 cm from the phantom surface.

When the phantom was scanned with the quadrature excitation, the temperature variations near the wire tips were recorded using a Neoptix ReFlex signal conditioner equipped with T1 fiber optic temperature sensors (Neoptix Inc, Quebec City, Canada). The fiber optic probes were placed in a specific way so as to ensure contact with the wire tips. The temperature data for each lead were obtained from different scans. To ensure a fair comparison, the gel phantom was kept in the refrigerator and allowed to reach the same initial temperature (5.5 °C). This low initial temperature, rather than the room temperature of 19 °C, was chosen to prevent the gel from melting because it would be exposed to high heat during the experiment. The rate of temperature increase caused by heat conduction from the surface was approximately 2 °C/hour, which was significantly lower than that caused by the applied electric field.

To obtain a linearly polarized excitation, one of the ports was disconnected. The orientation of the phantom was adjusted to make the location of the lead coincide with the zero electric field plane. Once the temperature data under this condition (minimum heating condition) was collected, the phantom was rotated 90 degrees to position the lead in the maximum electric field plane. Similar steps were taken for the measurement of curved wires.

In all of the experiments, a single temperature probe was used to eliminate probe calibration errors and measurement errors caused by improper probe placement.

3.4.2) Transmit Field Optimization

The linearly polarized birdcage coils may solve the RF heating problem of the implant leads. As previously mentioned, a linear birdcage coil can generate a whole-volume averaged SAR that is twice that generated by a quadrature birdcage coil, which may be unacceptable for certain applications. Therefore, alternative implant-friendly strategies that can guarantee similar or better MR image homogeneity need to be identified.

As previously mentioned, instead of designing novel coils, we tried to optimize the electric field distributions of currently available coils via simulation.

The optimization was conducted on a cylindrical head model with a conductivity of 0.5 S/m, relative permittivity of 70, diameter of 16 cm and length of 25 cm. Four separate optimum field solutions were computed under four different sets of conditions, as given below.

3.4.2.1) Quadrature birdcage coil

The field distribution of an ideal quadrature coil was obtained using the above-mentioned optimization algorithm but with no constraint on the electric field. In this calculation, only a single point at the center of the object was chosen as the point of interest. Due to angular symmetry, the solution contained a single circumferential mode that corresponded to the field of a forward polarized birdcage coil. The whole-head averaged SAR calculated using this method can be considered as the minimum SAR one can obtain with a birdcage coil.

3.4.2.2) Linear birdcage coil

The field of the linearly polarized birdcage coil was directly constructed from the previous solution by introducing a reverse circular polarization mode. The conjugates of the field expansion coefficients calculated for the quadrature coil were used for the reverse polarized mode. According to our theory, this solution should contain a zero electric-field plane. If this field coincides with the plane of the implant lead, no implant heating will be observed. Although this linearly polarized coil may be regarded as an implant-friendly coil, the whole-head average SAR obtained using this solution is twice as large as that of the quadrate birdcage coil. Therefore, a better solution is needed.

3.4.2.3) Implant-friendly coil

To minimize the electric field around the implant, the exact location of the implant lead needs to be known. For demonstration purposes, a 20-cm straight implant lead is assumed to be placed 1 cm away from the surface in the longitudinal direction (Figure 3.2).

32

(a) **(b)**
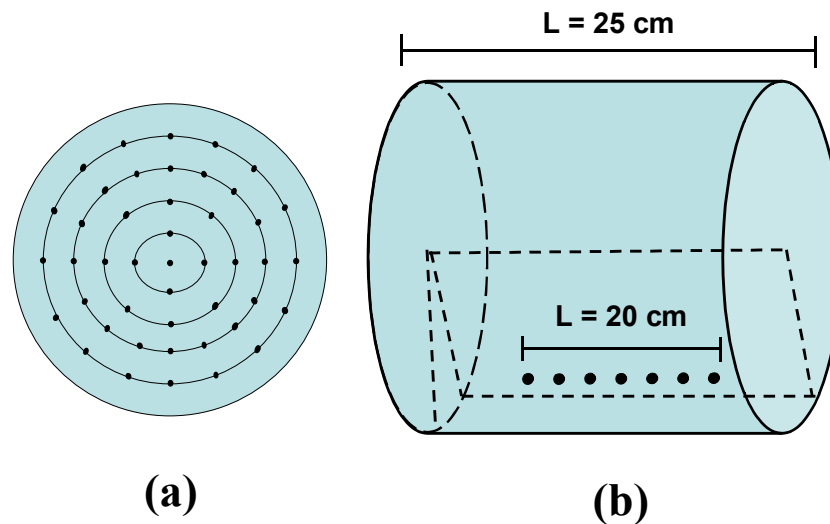
Figure 3.2 To ensure homogeneous excitation, the coil transmit sensitivity was constrained to unity at 45 sample points, forming a circular region with a diameter of 15 cm on the transverse plane (Panel a). The electric field was constrained to zero at seven sample points on a straight line whose distances to the phantom surface were 1 cm (Panel b).

Coil transmit sensitivities were chosen to be exactly the same as those for the linear birdcage coil. The optimization problem is solved by applying these transmit sensitivity values at sample points shown in Figure 3.2. The tangential component of the electric field was set to zero at sample points on a lead, as shown in Figure 3.2. This strategy guaranteed that the whole head average SAR would be either less than or at most equal to the SAR of a linear birdcage coil because the transmit sensitivity was preserved, but the electric field constraints were relaxed.

3.4.2.4) Implant-friendly homogeneous coil

In an MRI scan, it is usually desirable to obtain a homogeneous transmit sensitivity in the region of interest. To achieve this goal, the transmit coil sensitivity is constrained to unity at points in the transverse plane (Figure 3.2). The tangential component of the electric field was set to zero at sample points

on a lead (Figure 3.2). Results obtained from the above-mentioned experiments and simulations are given in the next section.

3.5 Results

3.5.1) Implant-Friendly RF Coil

Figure 3.3 shows the time course of the temperature increase near the tip of a straight wire in three different modes: the quadrature mode, the linear mode (maximum heating case) and the linear mode (minimum heating case). A temperature increase of 12.1 °C was observed at the tip of the wire for the quadrature case. For the maximum heating case of the linear mode, an increase of 24.7 °C was observed, For the minimum heating case of the linear mode, only a 0.8 °C difference was observed, which was significantly smaller than the difference observed for the quadrature case. For the curved wires, similar trends were observed, with temperature increases of 9.2, 19.1 and 0.3 °C observed for the three cases (Figure 3.4) Again the temperature change for the minimum heating case was significantly smaller than for the other two cases.
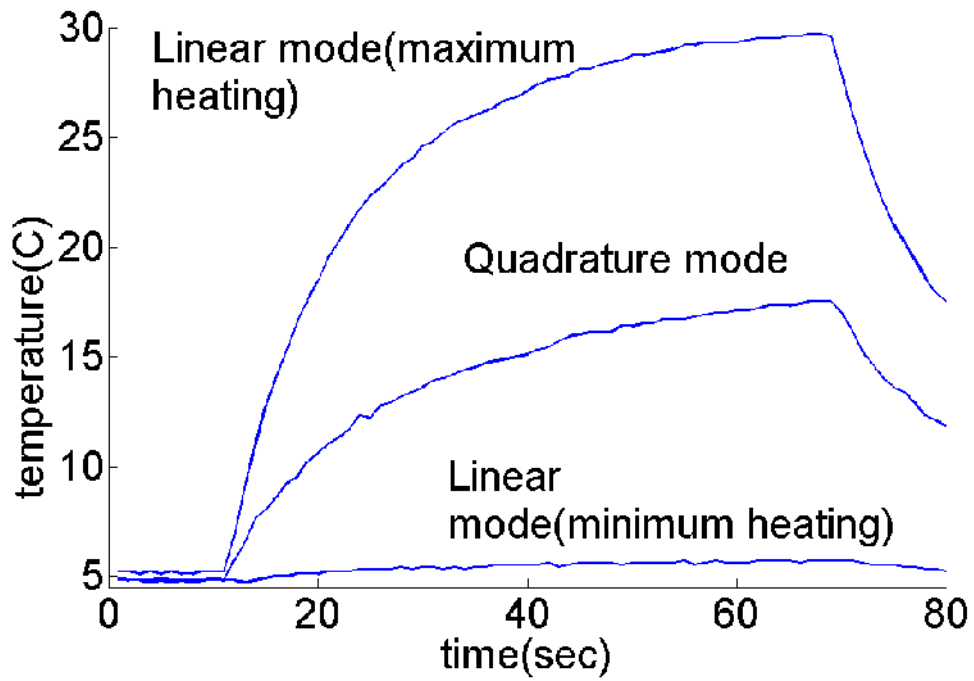
Figure 3.3 Temperature rise as a function of time measured for a straight wire with three modes: the minimum heating linear mode, the maximum heating linear mode and the quadrature mode. Final temperature increases of 0.8°C, 24.7°C, 12.1°C were observed with the minimum heating linear mode, the maximum heating linear mode and the quadrature mode, respectively.
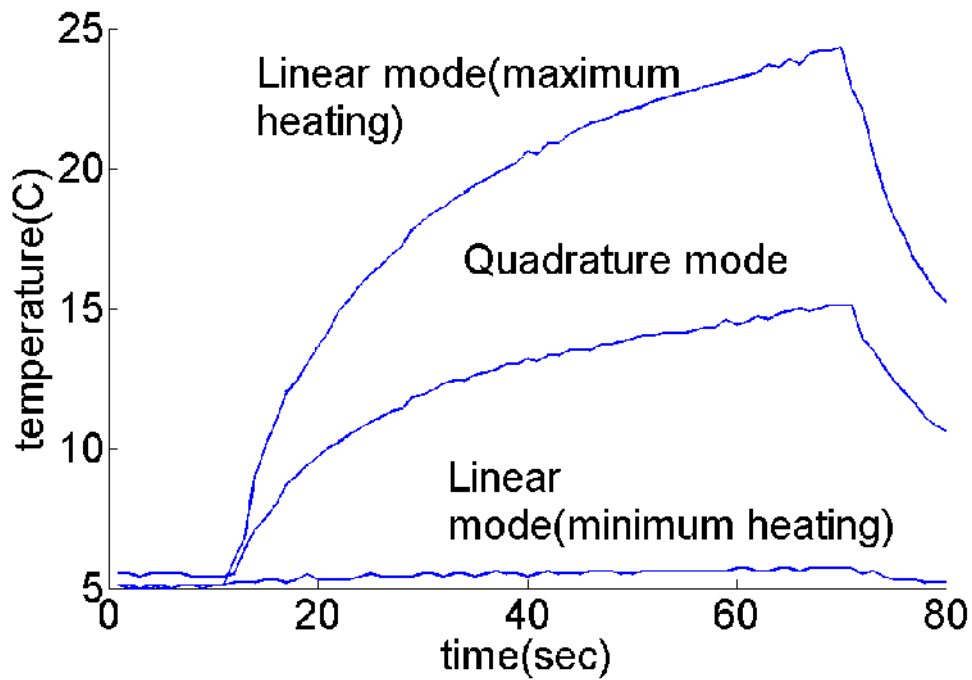
Figure 3.4. Temperature rise as a function of time measured for a curved wire with three modes: the minimum heating linear mode, the maximum heating linear mode and the quadrature mode. Final temperature increases of 0.3°C, 19.1°C and 9.2°C were observed with the minimum heating mode, the maximum heating linear mode and the quadrature mode, respectively.

3.5.2) Transmit Field Optimization

In order to alleviate the whole body SAR problem due to a linearly polarized birdcage coil, the problem can be solved in its most general form by minimizing the whole body SAR. The ranges of cylindrical mode index integers, m and n, were chosen as [-8, 8] and [10, 10], respectively. These ranges were determined by running a convergence analysis on the average SAR value. It was numerically found that increasing the range of m and n further, does not change the solution more than 5%. For transmit field optimization, four different optimum field solutions were simulated under four different conditions as described earlier. The transmit sensitivity of the mid-point is set to unity for all

simulations. A homogeneity coefficient was calculated for each field solution by averaging the difference between the sensitivity of each pixel and the mid point in the transverse plane. Note that a zero homogeneity coefficient represented a perfectly homogeneous transmit sensitivity profile

3.5.2.1) Quadrature birdcage coil

Figure 3.5 a shows the transmit sensitivity of the birdcage coil. The longitudinal components of the electric field on the trans-axial plane and on the "$\phi = 0$"half-plane are shown in Figures 3.5b and 3.5c. The resulting minimum whole-head average SAR was also calculated. Due to angular symmetry, this solution imposed a single circumferential mode that corresponded to a perfectly forward circular polarized field distribution. The whole-head average SAR value was defined as 1 au (arbitrary unit) in this case, which actually set the lower bound for the whole-head average SAR because H_f is constrained only to the origin. SAR values of the rest of the coils were defined accordingly. The homogeneity coefficient of this solution was found to be 0.41. As can be seen from Figure 3.5a, there is an approximately two-fold difference between the sensitivity at the center and at the periphery. This variation is due to the conductive losses in the sample and to the wavelength effects.

3.5.2.2) Linear birdcage coil

A linearly polarized field was obtained from the previous solution as explained earlier. Figure 3.5d shows the transmit sensitivity of the linear birdcage coil. The longitudinal components of the electric field on the trans-axial plane and on the "$\phi = 0$" half-plane are shown in Figures 3.5e and 3.5f. This field solution featured a zero electric field plane, which made it a safer choice in terms of RF implant heating for implants in this plane. The sensitivity was equal to 1 at the origin. The SAR value obtained by this field configuration was twice as much as that of the quadrature birdcage coil. The linear coil did not have the same transmit sensitivity as the quadrature coil, but its homogeneity coefficient, calculated as 0.46, was similar to that of the quadrature coil.

3.5.2.3) Implant-friendly coil

Figure 3.6a shows the sensitivity of the implant-friendly coil. The longitudinal components of the electric field on the trans-axial plane and on the "$\phi = 0$"half-plane are shown in Figures 3.6b and 3.6c. The longitudinal component of the electric field was forced to be equal to zero only around the implant lead.

However, as can be seen from the figures, the electric field was zero on the lead and close to zero at the rest of the $\phi = 0$ plane. The relaxed constraints on the electric field caused a decrease in the whole-head average SAR down to 1.49 au. The implant-friendly coil had a field solution that was very similar to the linear birdcage coil. The homogeneity coefficient of this solution, calculated to be 0.46, equaled that of the linear coil.

3.5.2.4) Implant-friendly homogeneous coil

Figure 3.6d shows the sensitivity of the implant-friendly homogeneous coil. The longitudinal components of the electric field on the trans-axial plane and on the "$\phi = 0$" half-plane are shown in Figures 3.6e and 3.6f. The whole-head SAR value obtained for this case was 2.96 au, which was significantly larger than those obtained from previous cases. On the other hand, the homogeneity coefficient of this solution was 0.0233, which implied the possibility of building an implant-friendly coil with close to perfect homogeneity. However, under this circumstance, an increase in the average SAR became unavoidable.

COIL SENSITIVITY

ELECTRIC FIELD IN
TRANSAXIAL PLANE

ELECTRIC FIELD IN
$\phi = 0$ HALF-PLANE

QUADRATURE COIL

(a) (b) (c)

LINEAR COIL

(d) (e) (f)
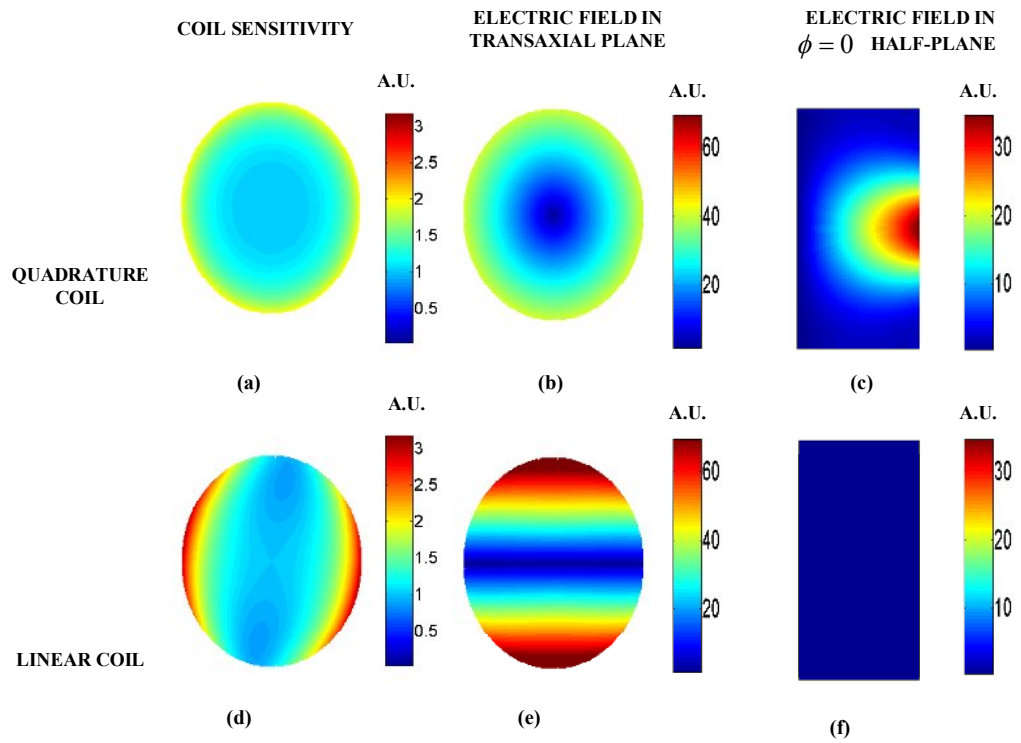
Figure 3.5 Transmit sensitivity (a, d), electric field in the trans-axial plane (b, e) and the longitudinal component of the electric field in the $\phi = 0$ half-plane (c, f) generated by quadrature and linear coils. Note that all field solutions are in arbitrary units.

COIL SENSITIVITY   ELECTRIC FIELD IN TRANSAXIAL PLANE   ELECTRIC FIELD IN $\phi = 0$ HALF-PLANE

IMPLANT FRIENDLY COIL

IMPLANT FRIENDLY HOMOGENOUS COIL
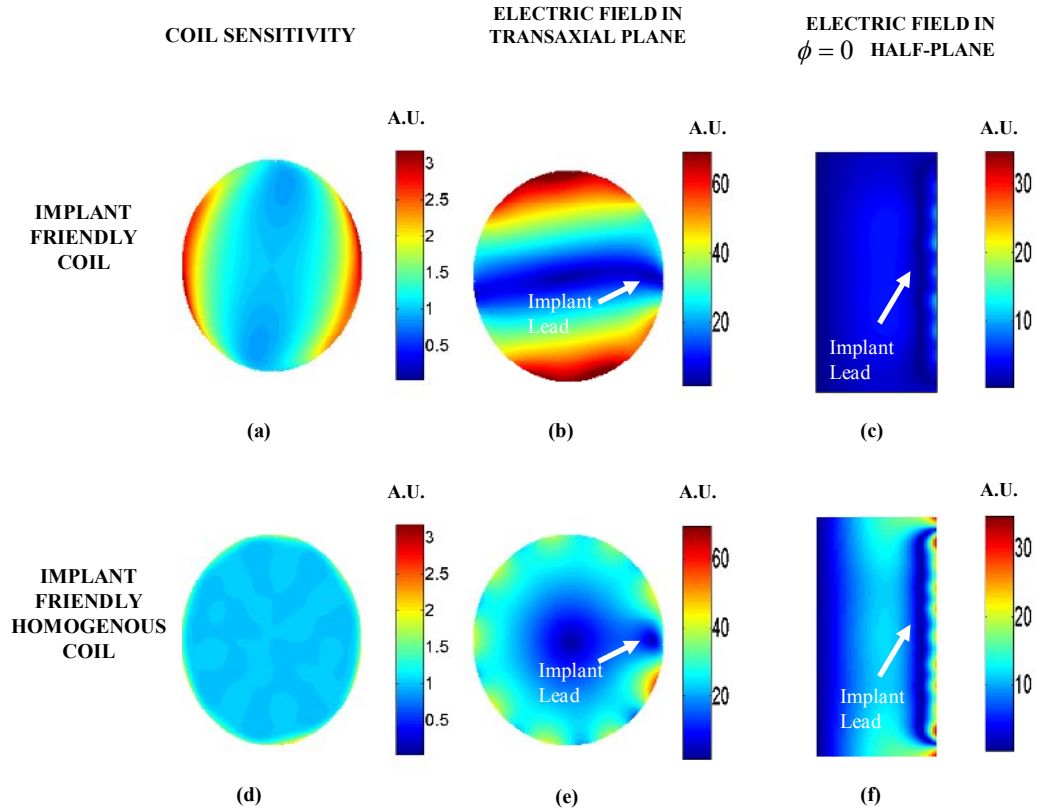
Figure 3.6 Transmit sensitivity (a, d), electric field in the trans-axial plane (b, e) and the longitudinal component of the electric field in the $\phi = 0$ half-plane (c, f) generated by implant-friendly coils and implant-friendly homogeneous coils. Locations of the implant lead are denoted by arrows in the figures. Note that all field solutions are in arbitrary units.

3.6 Discussion

It was shown in this study that a linear birdcage coil can be used as a transmitter coil in MRI and enable safe scanning of patients with implants. A linear birdcage coil has a transmit sensitivity similar to that of a quadrature birdcage coil. Moreover, the electric field distribution of the linear coil is zero at an angular plane, and any metallic implants placed at this plane will experience zero heating. The angle of this plane can be adjusted to any angle $\phi = \phi_0$ by

supplying appropriate excitation currents weighted as $\cos\phi_0$ and $\sin\phi_0$ in two ports of the linear birdcage coil. This task can be performed with a two-channel transmit array system, which is commercially available for some MRI scanners. In all the experiments and simulations, homogeneous cylindrical head models were used. For real-life situations, variations in tissue conductivity may introduce some errors into the field calculations. To prevent implant RF heating, regions free of electric fields need to be created around the implant. In this study, we successfully generated such regions using special implant-friendly coils such as a linear birdcage coil; however, the performance of these designs needs to be further tested in patients.

In this work, it was theoretically shown that it is possible to find a field distribution that minimizes RF heating of implant leads. This was experimentally shown for two specific lead geometries that was confined in a cylindrical plane. For arbitrary lead geometries, the applicability of the method should also be investigated experimentally

In a previous study [32], the electric field distribution of a linearly polarized coil was calculated for a head model, and the existence of the zero electric field region was demonstrated for field strengths up to 7.0 T. It was also shown that in the head model the linear excitation had a homogeneous transmit sensitivity in a 3.0-T scanner. However, when larger parts of the body such as the torso were imaged, this homogeneity could be reduced. To solve this problem, multi-channel excitation and RF shimming methods were proposed and investigated [37]. Although linear coils could solve the RF heating problem of implant leads in MRI, they caused twice as much average SAR as the quadrature coils. To reduce the SAR, computer simulations were performed. Instead of making a novel coil design, we calculated and optimized the field distributions of the coils, which provided us with important clues regarding the RF coil design. As can be seen from Figures 3.6 a, b, and c, the electric field of an implant-friendly coil is actually a slightly distorted version of the field of a linear birdcage coil. This finding indicates that a slight modification of the geometry of a linear coil can significantly reduce the whole-volume average SAR without sacrificing

41

homogeneity. An actual coil that has such field distribution characteristics needs to be built and further investigated.

The calculated field distributions can also be obtained using multi-channel transmit arrays. By controlling the currents in separate channels of a transmit array, the optimum field distributions can be approximated. As the number of the channels increases, the approximation will become more accurate. It is a new concept to use transmit arrays to reduce RF heating in implants. In the current study, we verified a similar concept using a linear birdcage coil, which can be directly applied to a two-channel transmit array system. However, the effectiveness of this multi-channel transmit array system remains to be investigated experimentally.

Knowing the location of the implant helps to reduce the average SAR. To locate the lead, the electric field near the implant can be set to zero, and low SAR scans can be performed prior to the examination. The obtained information can be further used to calculate the optimum excitation currents of a transmit phased array.

In this work the transmit field was optimized in order to reduce the RF heating of implants, and to obtain a uniform transmit sensitivity in the phantom. It should be noted that the transmit and receive problems are decoupled from each other. The receive chain can be optimized separately in order to achieve SNR enhancement, if necessary.

3.7 Conclusion

In this chapter, we showed that it is possible to modify the electric field distribution of a radio-frequency (RF) coil to generate electric field-free zones in the body without significantly altering the transmit sensitivity. As supported by our experimental data, a linearly polarized birdcage coil can be safely used to scan patients with implants. To further alleviate the problems caused by the doubling of the whole-volume average SAR, implant-friendly electromagnetic field solutions with the desired transmit sensitivity and minimum SAR were simulated.

4. REDUCTION OF RF HEATING OF METALLIC DEVICES USING A TWO CHANNEL TRANSMIT ARRAY SYSTEM

4.1 Introduction

The advent of interventional MRI made it possible to perform catheterization and biopsy procedures on patients under MRI guidance [14-16]. However, the risks related to the excessive heating of metallic devices have become a major safety concern in interventional MRI [17].

In general, for both diagnostic and interventional MRI procedures involving wire-shaped long conductor devices (catheters, biopsy needles, pacemakers, deep brain stimulators (DBS)), amplification of the specific absorption rate (SAR) at the device tip poses a potential risk for patients [13]. SAR amplification can cause excessive tissue burns if it is not reduced with appropriate methods. Many different methods have been reported for modifying the device geometry or adding lump circuit elements to the device to reduce the tip SAR amplification [18-21]. However, such modifications of the device geometry or circuitry could reduce mechanical robustness. In addition, for certain applications such as biopsy procedures, it is not convenient to modify the metallic needles with the above methods. Furthermore, for patients who carry MR incompatible devices, replacing the unsafe devices with the safer ones may not always be feasible.

In a previous study, we proposed a method based on the use of linearly polarized birdcage coils [24] to minimize RF heating at the wire tips. Because the electric field of the linear birdcage coil is equal to zero on an entire plane, the location of the metallic device was coincided with this plane, and the RF heating was reduced. Using this approach, it was shown that the homogenous transmit sensitivity characteristics were preserved. This method required steering the coil around the patient to coincide the implant with the zero-electric-field plane. At

3.0 Tesla, this technique worked well in uniform phantoms. However, tissue inhomogeneities can alter the electric field distribution in the body. In this case, knowing the coil geometry and the conductor currents in the coil may not be sufficient to estimate the location of the zero-electric-field plane. The shape of the zero-electric-field plane can be distorted, or its position can be shifted in a manner that is difficult to estimate. In general, when scanning patients with metallic devices using linear polarized excitation, monitoring the local electric field experienced by the metallic device is crucial. By doing so, the metallic device can be coincided with the zero-electric-field zone of the linear coil, and the patient can be scanned safely.

In the literature, many methods exist that are based on measuring RF-induced currents directly by attaching optoelectronic circuits to the conductor leads [29]. Although accurate measurements can be performed using these methods, when the modification of the metallic device is not possible, these approaches cannot be used non-invasively. There also exist other methods, in which the magnitudes of the RF currents on the metallic wires are calculated from their artifacts in MR images [38]. These artifacts can be used to monitor the level of RF-induced currents on the leads as well.

In another study [39], transmit arrays were used to control the induced currents on a guide-wire conductor; the relationship between the excitation voltages and the induced currents on the lead was modeled as a linear system, and the null space of the excitation matrix was computed. This approach enabled the induced current to be set to zero on the lead. However, in that work the flip angle distribution in the body due to transmit array excitation was not considered. The excitation that minimizes the induced current on a lead should also be convenient to perform imaging with a homogenous sensitivity pattern.

In this study, we used a birdcage coil as a two-channel TX array system to reduce the local SAR near the tip of metallic leads. By changing the magnitude of the excitation currents on two separate channels of the TX array, the electric field pattern was modified inside the body in order to find a safe excitation pattern that minimizes RF current artifacts near the lead tip. To monitor the

44

current, the image artifacts in the vicinity of the lead tips were measured. Phantom experiments were performed with copper wires and DBS leads. For convenience, an animal experiment was performed with copper wire only. By performing temperature measurements with fiber optic probes, it was shown that the device tip temperatures were reduced substantially with respect to standard quadrature excitation. It was shown that, for some lead geometries, linear polarized excitation can be used to reduce the local SAR. With linear excitation, the flip angle distribution and the overall image quality can be preserved compared to quadrature excitation. Finally, for some other lead geometries, elliptical polarization could be required to reduce the local SAR at the tip.

4.2 Theory

The electric field distribution in an infinitely long cylindrical object due to linear excitation can be expressed as follows [24]:

$$E_z = -H_f j\omega\mu_0\rho\sin\phi, E_\phi = 0, E_\rho = 0 \qquad (24)$$

In the above equation, H_f is the transmit sensitivity of the coil; E_z, E_ϕ and E_ρ are the longitudinal, angular and radial components of the electric field, respectively; ω is the Larmor frequency; ε and μ_0 are the permittivity and the permeability, respectively; ϕ and ρ are the angular and radial coordinates in the cylindrical coordinate system, respectively; and j is the imaginary number defined by $\sqrt{-1}$.

For this field distribution, the electric field is equal to zero on the entire $\phi = 0$ plane. This field can be generated by a linear birdcage coil that has a feed point at the $\phi = \pi/2$ plane. Similarly, a linear birdcage coil with a feed point at $\phi = 0$ and a zero-electric-field plane at $\phi = \pi/2$ would have a field distribution as in the following expression:

$$E_z = -H_f j\omega\mu_0\rho\cos\phi, E_\phi = 0, E_\rho = 0 \qquad (25)$$

To obtain a zero-electric-field plane at $\phi = \phi_0$, the electric field distribution should be equal to the following:

$$E_z = -H_f j\omega\mu_0\rho\sin(\phi - \phi_0), E_\phi = 0, E_\rho = 0 \qquad (26)$$

Using simple trigonometric identities, it can be shown that the above distribution can be expressed as the weighted sum of the two distributions in Equations 1 and 2.

To physically realize this field, a standard birdcage body coil should be used as a two-channel transmit array system. Let the fields generated by channel 1 and channel 2 be expressed by Equations 1 and 2, respectively. Then, the field distribution shown in Equation 3 can be realized by weighting the excitation currents of channel 1 and channel 2 with $\cos\phi_0$ and $\sin\phi_0$. In this case, a metallic lead with a shape that is confined inside the $\phi = \phi_0$ plane will experience zero electric field (Figure 1a). Therefore, no current will flow on the lead conductor. Similarly, for leads that extend slightly out of the zero-electric-field plane, the induced current on the lead can be made very small (Figure 1b).

This result can also be viewed from a different perspective by exploiting the linearity between the induced current and the transmit array excitation voltages. Let the currents induced on the lead due to the excitations of channel 1 and channel 2 be I_1 and I_2, respectively. Then, the total current due to a linear excitation using angle θ would be equal to $I = \cos\theta \cdot I_1 + \sin\theta \cdot I_2$. In this case, by choosing $\theta = \tan^{-1}(-I_1 / I_2)$, the current near the lead tip can be set to zero. Note that this solution requires that I_1 and I_2 have the same phase. The phase difference between I_1 and I_2 depends on many things, including the medium EM parameters and the orientation and the position of the lead with respect to the coil. A field due to a linear excitation has a constant phase and magnitude in an angular plane. Therefore, for a lead that is confined in a cylindrical plane,

I_1 and I_2 have the same phase. For the case in which I_1 and I_2 have different phases, the value of θ would be complex.

<div align="center">(a)   (b)</div>
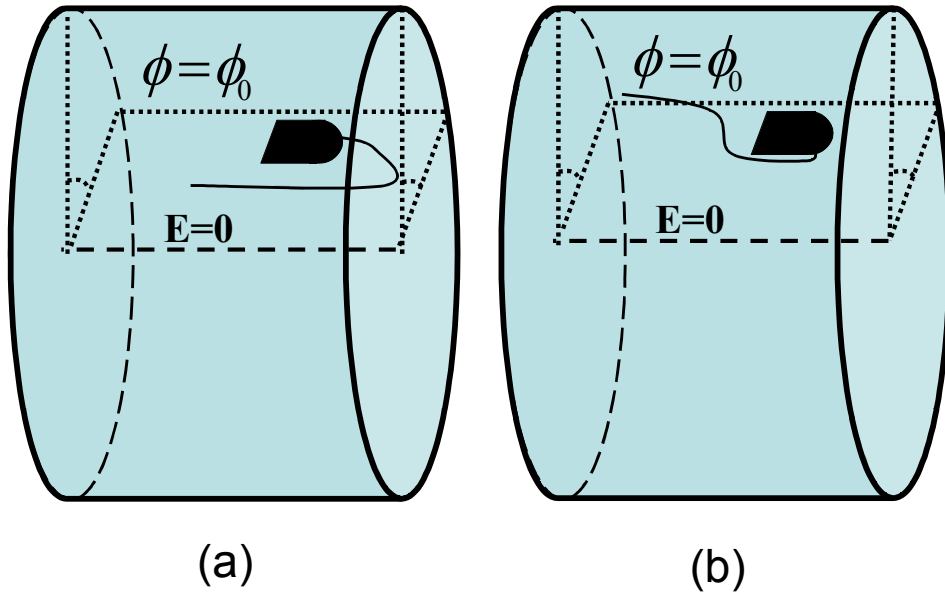
Figure 4.1 A metallic lead with a shape that is confined inside the $\phi = \phi_0$ plane experiences zero electric field. Therefore, no current flows on the lead conductor (Panel a). Similarly, for leads that extend slightly out of the zero-electric-field plane, the induced current on the lead can be made very small (Panel b).

When the leads are not confined in cylindrical planes but in large cylindrical volumes, as shown in Figure 2, I_1 and I_2 may have different phases. Therefore, linearly polarized excitation may be insufficient to completely reduce the tip current. In that case, the value of θ would be complex, and it would require using a different polarization to cancel the tip current. From an EM field distribution perspective, if a lead is not confined to the zero-electric-field plane, it could experience electric fields that are high enough to induce currents in the lead tip. In that case, a linear excitation may not be sufficient to completely cancel the lead tip current. Under all conditions, the induced current near the tip of a metallic lead can be made to be zero by using a two-channel excitation.
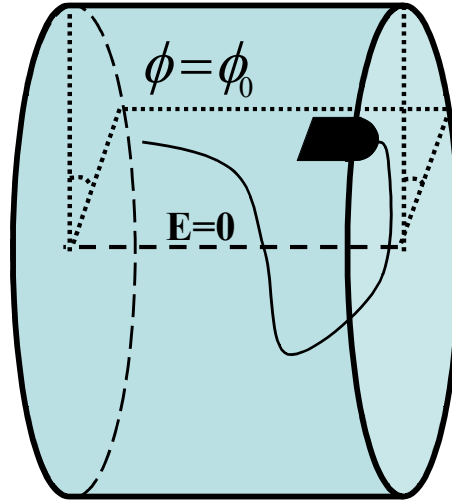
Figure 4.2 A metallic lead may have a shape that is confined in a large cylindrical volume. In that case linearly polarized excitation may be insufficient to completely reduce the tip current.

4.2.1) Monitoring Induced RF Current Artifacts

To reduce the currents induced by metallic devices, a method based on monitoring the signal intensity of the RF-induced artifacts is proposed. The relationship between the magnitudes of the RF-induced current and the artifact signal intensity is derived.

For a gradient echo sequence, the signal intensity due to a given flip angle α can be written as follows [38]:

$$S = \frac{c \cdot \sin(\alpha) \cdot (1 - e^{-TR/T1})}{1 - e^{-TR/T1} \cos(\alpha)} \tag{27}$$

In this equation, T1 and TR are the longitudinal relaxation parameter of the tissue and the repetition time of the GRE sequence, respectively. c is a factor that represents the local spin density and the sensitivity of the receiver coil.

To obtain linear excitation, the currents on the two channels of the transmit array should be weighted with $\cos\theta$ and $\sin\theta$, where θ is an arbitrary angle in

the interval $[0,\pi]$. Let $I[\theta,\phi_0]$ denote the relationship between θ and the tip current of the metallic lead located in the $\phi = \phi_0$ plane. If the nominal flip angle in the body due to the RF coil excitation is small, then the flip angle near the lead tip will be linearly dependant on the induced current; hence $\alpha = A \cdot I[\theta,\phi_0]$. If the flip angle α due to the RF-induced current is also small, by substituting $\sin\alpha \simeq \alpha$ and $\cos\alpha \simeq 1$ in Equation 4, the signal intensity can be approximated with the following expression:

$$S = c \cdot A \cdot I[\theta,\phi_0] \qquad (28)$$

Equation 5 shows that, to minimize the RF current at the tip of a lead located in the $\phi = \phi_0$ half plane, its artifact should be minimized by choosing the appropriate TX array excitation angle θ. By monitoring the magnitude of the RF current artifact near the lead tip, the excitation pattern that satisfies the above condition can be determined.

4.2.2) Finding a Safe Excitation Pattern

The magnitude of the artifact signal intensity due to a linear excitation can be written as follows:

$$S = \cdot \left| S_1 \cos\theta + S_2 \sin\theta e^{j\beta} \right| \qquad (29)$$

In this equation, S_1, S_2 are the magnitudes of the induced current artifact signals due to the excitations of channel 1 and channel 2, respectively. β is the phase difference between induced currents I_1 and I_2. To find a safe excitation pattern, the total signal intensity S should be set to zero. For this purpose, S_1, S_2 and β should be estimated by measuring S for different θ values. The S_1, S_2 and β values that minimize the mean square error between the theoretical and measured signal intensities can be found for this purpose. Once S_1, S_2 and β are

49

known, the channel 1 and channel 2 excitation currents can be weighted with $\cos\theta_0$ and $\sin\theta_0 \cdot e^{-j\beta}$ to achieve safe excitation, where $\theta_0 = \tan^{-1}(-S_1/S_2)$. Note that for the case in which $\beta = 0$, the safest excitation pattern is a linear excitation. In that case, by examining the measured signal intensity data, the safe excitation pattern angle can be found as the point where $S = 0$.

Using a linear polarized excitation guarantees that the flip angle distribution in the center is preserved. For leads that are confined in cylindrical angular planes, the safest two-channel excitation pattern is a linear excitation. However, for leads that are confined in large cylindrical volumes, the solution may have a different polarization.

4.3 Experiments

4.3.1) Phantom Experiments

To demonstrate the proposed theory, phantom experiments with copper wires and a commercial DBS lead (Medtronic 33877 DBS electrode, Medtronic Inc, Minneapolis, MN) were performed. A phantom body model of 20 cm in diameter and 30 cm in length was prepared with commercially available gel (Dr. Oetker Jello, Izmir, Turkey). To measure the conductivity and relative permittivity, a method based on cylindrical transmission line setup measurements was used. A conductivity of 0.5 S/m and a relative permittivity of 70 were obtained with 2.5 g/l of salt in the gel solution [36].

Copper wires and the DBS lead were placed in the phantoms, as shown in Figure 3. As demonstrated in the figures, the copper wire and the DBS lead had a shape that slightly extended out of the cylindrical angular plane. In Figure 3c, a copper wire with a helical geometry was used, which was confined in a larger cylindrical volume.
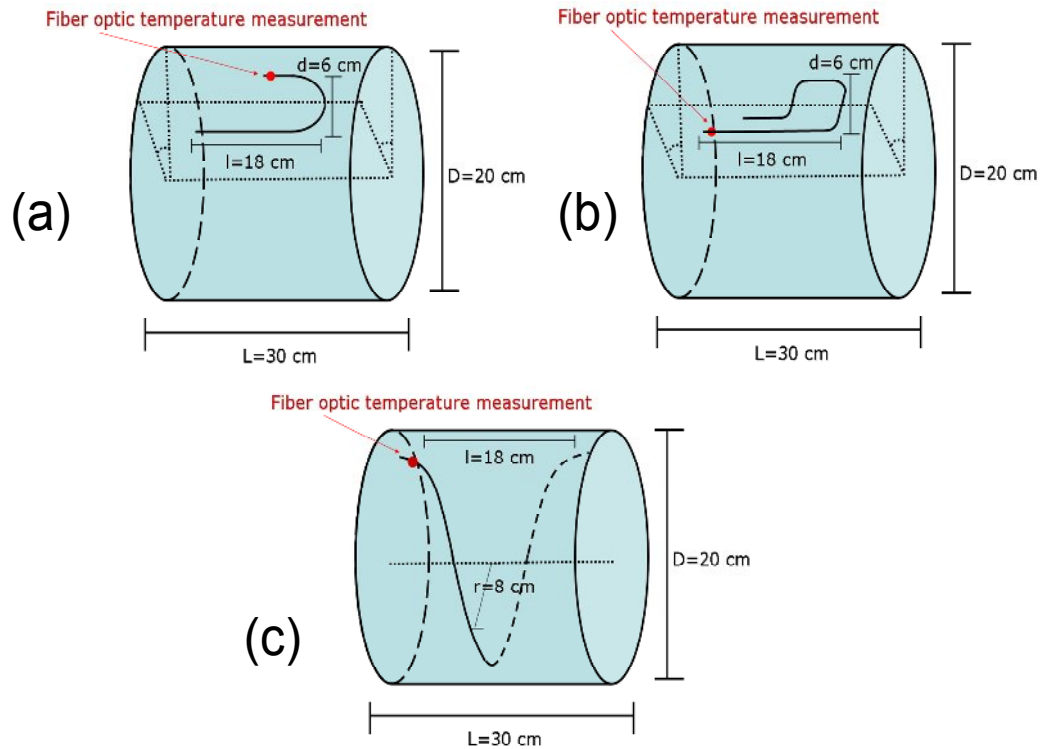
Figure 4.3 Copper wire and DBS lead in in Panel a and Panel b have a shape that slightly extends out of the cylindrical angular plane. The copper wire in Panel c is confined in a larger cylindrical volume.

The body coil of the Siemens 3.0 T Trio system was used in all experiments in the two-channel TX array mode. The phantoms with copper wire and DBS lead were scanned using a gradient echo sequence with a TR of 200 msec and a flip angle of 2 degrees. To monitor the magnitude of the artifact due to the RF current in the vicinity of the lead tip, a transverse image was obtained. For all cases, a small flip angle and a large TR were chosen so that the SAR value of the sequence was kept at a low level and no significant heating was expected near the lead tips.

The sequence was run using different linear excitation patterns with the TX array. The amplitudes of the currents in channel 1 and channel 2 were weighted with $\cos\theta$ and $\sin\theta$ to control the electric field distribution inside the phantom.

The value of θ was varied within the interval $[0, \pi]$ with a step size of $\frac{\pi}{36}$. A total of 37 images were obtained for each experiment. In every image, a region of interest (ROI) of 2 cm in diameter was selected around the lead tip to measure the maximum magnitude of the RF current artifact. Measurements were repeated for copper wire and DBS leads as explained above.

For all experiments, the safest two-channel excitation pattern was found. This pattern was used to scan the phantom with a high SAR sequence. A GRE sequence with a 4-msec TR was used for this purpose.

To calculate the peak SAR, the initial slope of the temperature rise at a depth of a 1 cm from the phantom surface was measured and then multiplied by the specific heat capacity of the gel. The heat capacity of the gel was determined to be 4100 J/kg/deg using the KD2 Pro Thermal Properties Analyzer (Decagon Devices Inc, WA, USA). The peak SAR was calculated as 4.4 W/kg.

For temperature measurements, a signal conditioner (Neoptix ReFlex) with fiber optic temperature sensors (Neoptix Inc, Quebec City, Canada) was used. The temperature variations at the wire/needle tips were recorded.

After the scan, the gel phantom was kept in the refrigerator for 10 minutes to ensure that the temperature reached a steady state of 5.5 °C. All phantom experiments started at a low initial temperature to prevent the gel from melting due to high temperatures near the lead tips. Afterward, the phantom was placed in the scanner, and the channel currents were adjusted to obtain standard quadrature excitation. For this purpose, the magnitude of the currents on channel 1 and channel 2 were weighted with unity, and the phases were set to 0 and $\pi/2$, respectively. Then, the phantom was scanned once more with the quadrature excitation pattern. The temperature variations near the lead/needle tips were recorded similarly. The experiments were repeated with the copper wire and DBS leads with the configurations shown in Figure 3.

4.3.2) Animal Experiments

To demonstrate the effectiveness of the method, an ex vivo swine experiment was performed. A copper wire was placed under the skin and muscle tissue of a pig. The dimensions of the wire were chosen to be the same as those of the wire used in the phantom experiment. First, a rectangular region approximately 1 cm deep was cut from the abdominal wall of the animal. Then, the copper wire and the temperature probe were placed under the cut section, as shown in Figure 4.
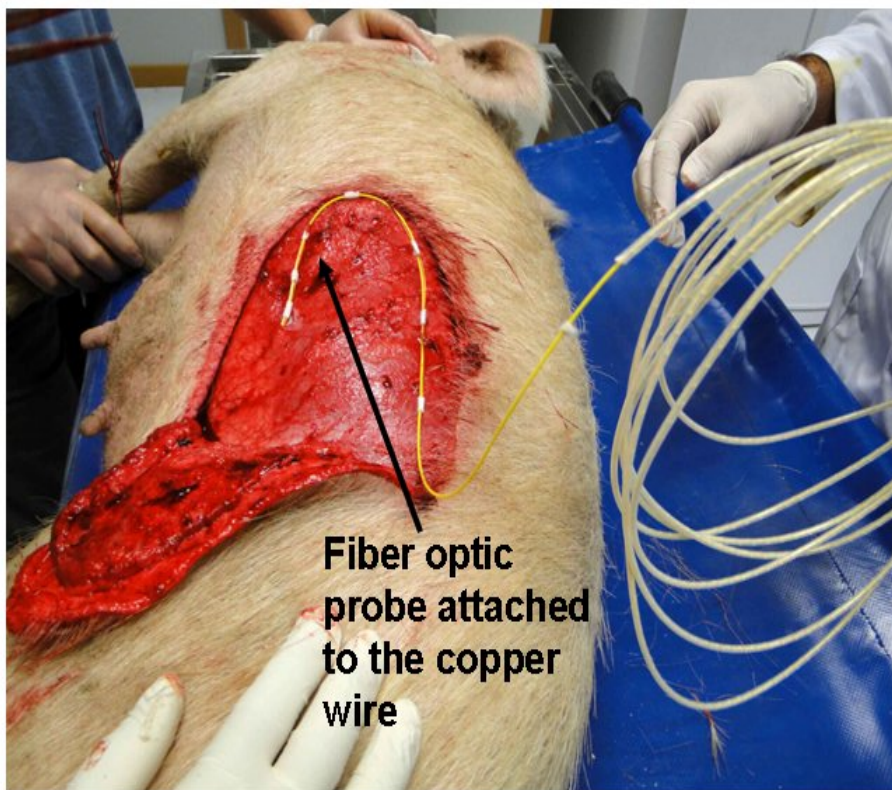
Figure 4.4 A rectangular region approximately 1 cm deep was cut below the chest of the animal. Then, the copper wire and the temperature probe were placed under the cut section, Finally, the muscle and the skin layer were sewn back in place to cover all parts of the copper wire with living tissue.

Then, the muscle and the skin layer were sewn back in place to cover all parts of the copper wire with living tissue.

The same procedures used for the copper wire-phantom experiments were repeated for the animal experiments.

4.3.3) Patient Experiments

In order to prove that the method can be used to obtain clinical images, the safe excitation patterns found in phantom and animal experiments in section 3.2 and 3.3 are used to scan volunteers. For this purpose the channel 1 and channel 2 excitation currents were weighted with $\cos\theta_0$ and $\sin\theta_0 \cdot e^{-j\beta}$ by using the θ_0 and β values obtained from the phantom experiments.

GRE sequence with TR of 100 msec and a flip angle of 25 degrees.is used to obtain brain images of a 30 year old male volunteer. The resulting images are compared to an image obtained with a standard quadrature pattern.

4.4 Results

4.4.1) Phantom Experiments

MR images of the phantoms with copper wires and DBS leads were obtained as explained in the previous section. Thirty-seven images were obtained for each experiment using θ values of $[0, \frac{\pi}{36}, ..., \pi]$. The maximum value of the artifact in a circular ROI around the lead was measured for each excitation pattern. Then, the S_1, S_2 and β parameters were estimated, and the theoretical artifact signal intensity curve that best fit the measured data was drawn. Figure 5 and Figure 6 shows the theoretical and measured signal intensity curves with respect to θ for copper wire and DBS leads.
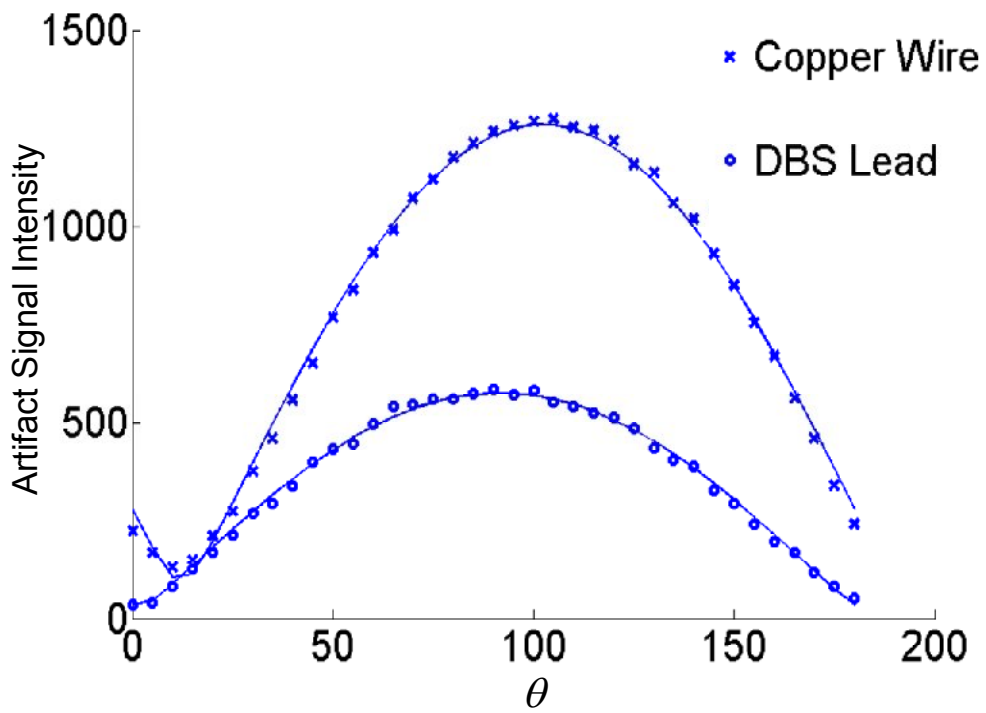
Figure 4.5 Theoretical and measured signal intensity curves of copper wire and DBS lead which was shown in Figure 4.3, Panel a and Panel b.
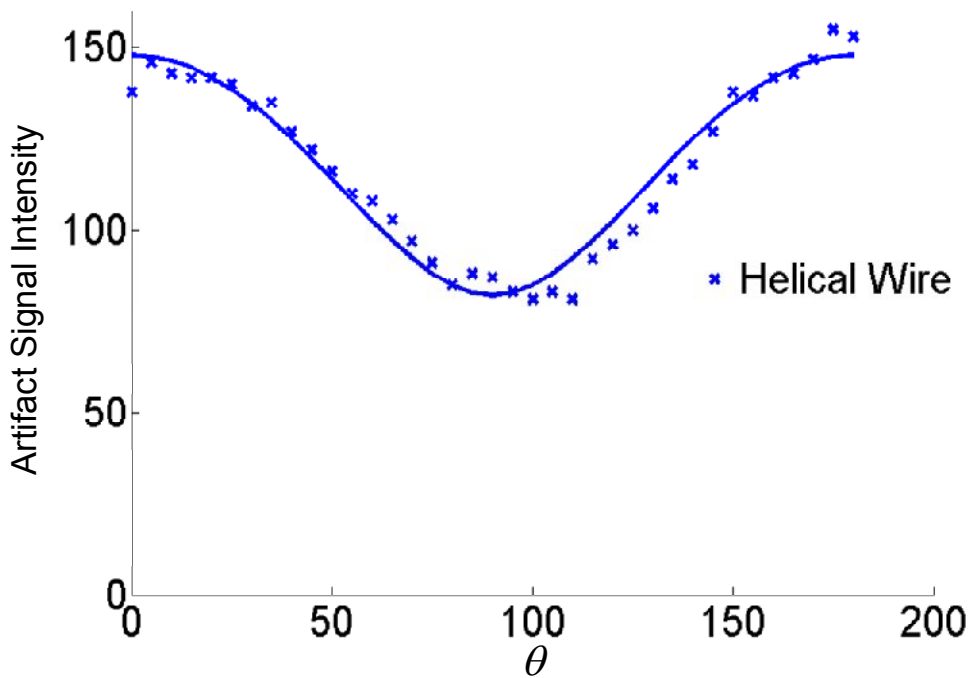
Figure 4.6 Theoretical and measured signal intensity curves of copper wire which was shown in Figure 4.3, Panel c

The calculated β values for the DBS lead, copper wire, and helical DBS lead were found to be $-10^0, 16^0$ and 85^0, respectively. Notably, the β values for copper wire and DBS lead were close to zero, which shows that practically the safest two-channel excitation is the linear excitation for these lead geometries. Furthermore, the minimum point for the artifact intensity curves for these experiments was close to zero. However, for the helical lead experiment, the β value was much different than 0, showing that the safest two-channel excitation is elliptically polarized for this lead geometry. After S_1, S_2 and β were found for each experiment, the channel 1 and channel 2 excitation currents were weighted with $\cos\theta_0$ and $\sin\theta_0 \cdot e^{-j\beta}$ to achieve safe excitation, where $\theta_0 = \tan^{-1}(-S_1 / S_2)$. The θ_0 values for copper wire, DBS leads and helical copper wire experiments are obtained as 5, 20 and 60^0 respectively.

Using these safe excitation patterns, each phantom was scanned using a high SAR sequence, as mentioned in Section 3.1. Then, each phantom was also scanned by using a quadrature excitation pattern. The temperature variations near the lead tips were recorded using a signal conditioner with fiber optic temperature sensors. The maximum tip temperature for each phantom experiment is shown in Table 1. Notably, using the safest excitation pattern reduced the tip temperature substantially with respect to that of the quadrature excitation.

Maximum Lead Tip Temperature (C)	Safest 2 Channel Excitation	Quadrature Excitation
Copper Wire (Phantom)	**0.2**	**13.8**
DBS Lead	**0.2**	**12.7**
Helical Copper Wire	**0.3**	**4.9**
Copper Wire (Animal Experiment)	**0.2**	**5.5**

Table 2 Maximum tip temperature is shown for each experiment. Notably, using the safest excitation pattern reduced the tip temperature substantially with respect to that of the quadrature excitation.

4.4.2) Animal Experiments

Animal experiments were performed on a pig, as explained in Section 3.2. Similarly, the maximum magnitude of the RF current artifact inside the ROI was plotted with respect to θ in Figure 7. The β value was calculated to be -10^0 for this experiment. Because β is almost zero, linear excitation can be used as the safest excitation pattern in this condition. The minimum current artifact was obtained with the value of $\theta = 15^o$. The pig was scanned using the safest excitation pattern and with the quadrature excitation pattern using the same high SAR sequences that were used in the phantom experiments. Table 1 shows the maximum temperature increase in the lead tip for both the quadrature and safe excitation patterns for both the phantom and the animal experiments. The tip temperature was reduced substantially with safest excitation patterns when compared to quadrature excitation.
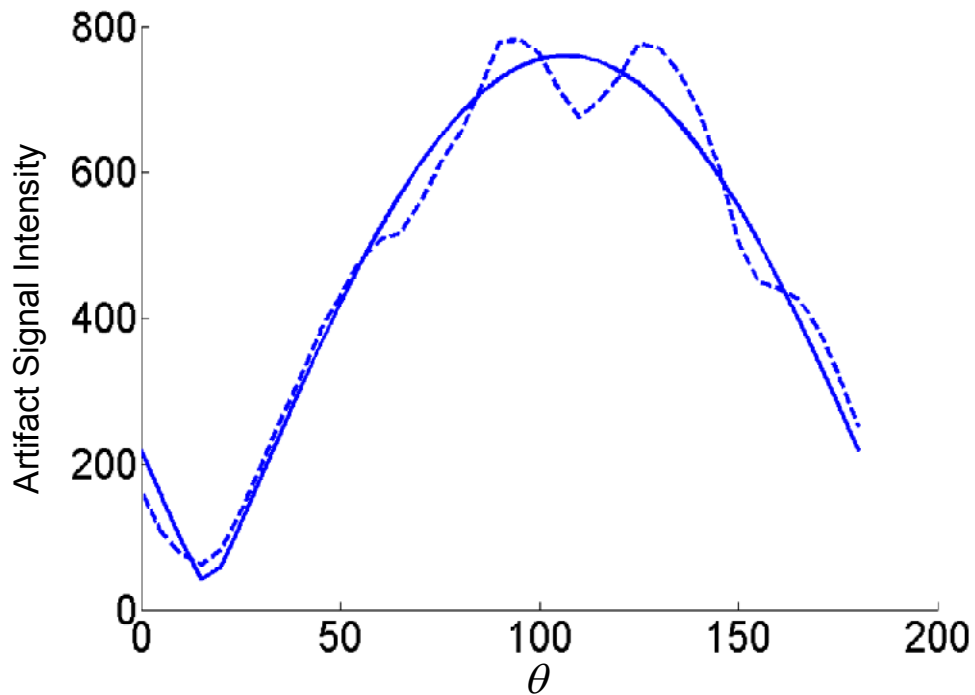
Figure 4.7 Theoretical and measured signal intensity curves of copper wire used in animal experiment.

4.4.3) Patient Experiments

GRE images obtained with the quadrature and the safe excitation patterns are shown in Figure 8. The sequence parameters were chosen as; Flip Angle=25 deg, TR=350 msec, TE=4 msec. Panel a shows the image obtained by a quadrature excitation. By using the safe excitation patterns, RF field homogeneity was not disturbed significantly. By visual inspection it can be seen that all images have similar image homogeneity. The flip angle at the center of the images were preserved with the safe excitation patterns using $\theta = 5$, $\beta = -10^{\circ}$ (Panel b)and $\theta = 20$, $\beta = 16^{\circ}$ (Panel c). For $\theta = 60$, $\beta = 85^{\circ}$ case (Panel d) the flip angle at the center of the image was reduced slightly as it can be seen from the image.
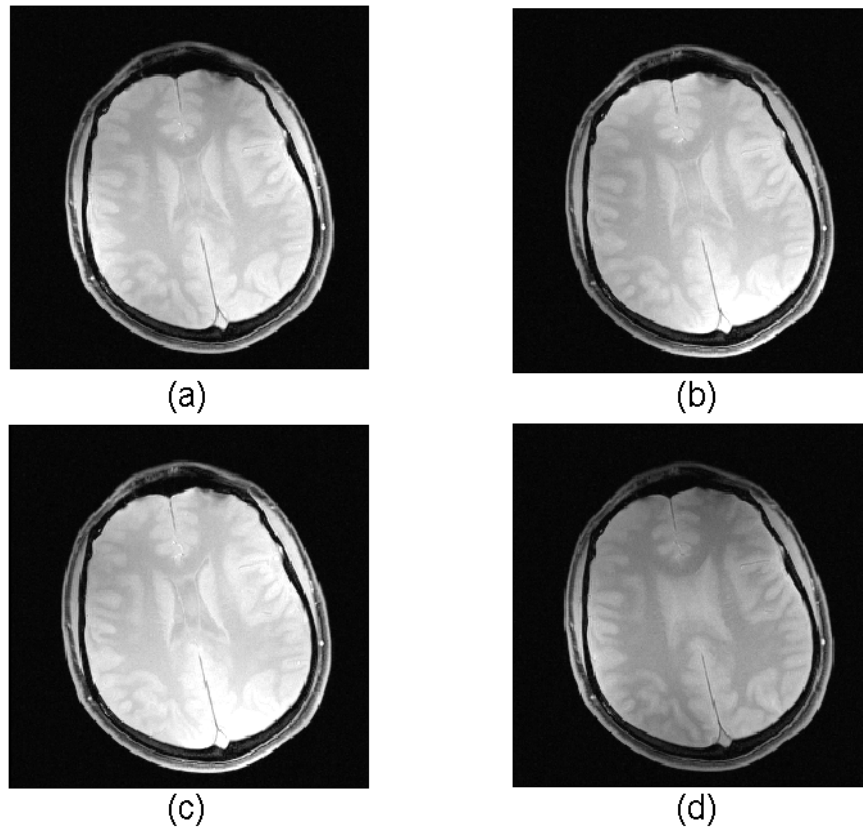
Figure 4.8 Brain images obtained with the quadrature (Panel a) and the safe excitation patterns (Panel b,c,d), using GRE sequence. $\theta = 5$, $\beta = -10^{o}$ was used in Panel b, $\theta = 20$, $\beta = 16^{o}$ was used in Panel c, $\theta = 60$, $\beta = 85^{o}$ was used in Panel d. The sequence parameters are; Flip Angle=25 deg, TR=350 msec, TE=4 msec. By visual inspection it can be seen that all images have similar image homogeneity.

4.5 Discussion

A method is herein proposed to reduce the RF heating of the metallic devices using a two-channel transmit array system. The proposed method was tested with phantom and animal experiments. In all cases, the tip SAR at the end of the metallic devices was reduced substantially without causing a significant image quality degredation.

A GRE sequence was used to measure the RF current artifacts near the lead/needle tips. By changing θ at intervals of $\pi / 36$ within the range of $[0, \pi]$,

a safe transmit array excitation pattern was found. Each sequence lasted for 12.8 sec, and the total of 36 sequences lasted for 7 min. θ can be covered in a smaller range or with a larger angular step size, thus reducing the measurement time significantly. However, by doing so, the accuracy in finding the safest excitation pattern would also be reduced.

After the safest two-channel transmit excitation pattern is found, the same pattern can be used in other sequences as long as the position of the metallic device is not changed. This condition would be valid for patients with implants, given that location of the implant does not change with respect to the coil during the scan. For interventional procedures, in which the device is bound in a thin cylindrical slice and for which the location is known prior to the scan, a single excitation pattern could be adequate.

A GRE sequence was used to monitor the RF current artifacts because of the simplicity it offers in formulation and analysis. Faster sequences with shorter TR and multi RF excitations can also be used to monitor RF current artifacts. The local SAR at the device tip that can be caused by these sequences should always be considered.

The method was tested in vivo an ex vivo animal experiment, and it was shown that the tip temperature can be reduced even in inhomogenous objects. However, the effect of motion artifacts should be considered for clinical studies. Since the signal intensity of the artifact can be effected from the movements of the transmit/receive coil, respiratory gated sequences may be used to solve this issue.

In the cases analyzed in this study, the currents induced on the lead generated a non-zero transverse magnetic field. In some cases, the magnetic field due to the current may be in the longitudinal direction. To measure the variation of the artifact with respect to θ, an imaging plane should be chosen such that the induced magnetic field has a non-zero transverse component in the imaging plane. In this study, the imaging plane was always chosen as the transverse plane. For different lead orientations, the transverse plane may not always be the most appropriate imaging plane.

By finding the safest two-channel transmit array excitation pattern, the current near the tip of the lead is minimized. At some other location on the lead, the RF current may be non-zero. The tip point is the most critical point where the local SAR should be minimized. The other end of the lead is either terminated with the implant case or simply extends outside the body, as in interventional procedures. The local SAR at the shaft of the device/lead is also significantly less than the tip SAR, as shown by many studies. Therefore, in this study, the effect of minimizing the current and the local SAR near the lead tip was investigated.

The use of linear excitation enabled the preservation of the flip angle distribution with respect to quadrature excitation in the center of the body. However, two-channel excitations other than quadrature or linear excitation may cause reductions in flip angle and RF field homogeneity. This effect can be more significant in higher field strengths. Multi-channel TX array excitation can be used to overcome these problems [25]. An excitation pattern that guarantees SAR reduction at the tip of the device and generates a uniform transmit field in the body should be calculated for this purpose. The currents on each channel of the array should be chosen appropriately to achieve the above-mentioned task. However, it should be noted that as the number of channels increases, the pre-scan time required to calculate a safe excitation pattern increases. The contribution of each array element to the transmit field and the tip current on the lead should be modeled separately. Then, an optimization problem that takes all of these parameters into account should be solved before scanning each patient.

4.6 Conclusion

We demonstrated a method to reduce the RF heating of metallic devices with transmit array systems. The artifacts that result from RF-induced currents on the metallic leads and needles were monitored to find the safest excitation pattern with a two-channel transmit array system. As a result, heating at the tip of the metallic devices was reduced significantly, as shown by both phantom and animal experiments.

5. REDUCTION OF RF HEATING OF METALLIC DEVICES THROUGH MULTI-CHANNEL EXCITATION

5.1 Preface

The content of this chapter has been presented (in part) in a conference publication, reference: Eryaman Y., Demir T, Atalar E "Reduction of RF Heating of Metallic Devices Using Transmit Arrays" Proc Intl Soc Mag Reson Med 18(2010)**:3883.**

5.2 Introduction

In this chapter, the reduction of the RF heating of metallic devices is demonstrated by using multi-channel excitation. In the previous chapter, a similar problem was solved by using a two-channel transmit array.

The concept of steering the linear polarized electric field works when there are no volume-average SAR and transmit field homogeneity constraints. However, for certain applications, these issues can be significant. The two-channel excitation, although reducing the RF heating on lead, may not be sufficient to obtain a uniform transmit sensitivity during whole body imaging, especially at the high field strengths. Furthermore, with linear excitation, the average SAR is doubled and the peak SAR is quadrupled with respect to quadrature excitation.

With multi-channel TX arrays, the phase and magnitude of the currents on separate channels of the transmit coil can be chosen to satisfy a given SAR and field homogeneity constraint. In addition to those, the local electric field distribution can also be controlled for reduction of the heating of metallic devices. The main goal of the work presented here was to obtain a homogenous transmit field distribution with a minimum average SAR, with the condition that the metallic device inside the body experiences zero or minimal electric field.

5.3 Theory

By choosing the excitation current pattern similar to the currents in the legs of a linear birdcage coil, the RF heating of a metallic device can be reduced. The excitation pattern for a linearly polarized field is given as $a_i = A\sin(2\pi i / N - \phi_0)$, where i is the index of the channel carrying the current, a_i (1<i<N), and ϕ_0 denotes the angular position of the plane on which the metallic device is located; N is the number of channels in the transmit array. The heating extension of the device can have a shape of arbitrary geometry, including loop structures. As long as the shape is bounded in a thin angular slice, the heating can be minimized. The main concern with this approach is that the average SAR is doubled with respect to a quadrature excitation. To solve this issue, the current excitation pattern should be modified in order to minimize the average SAR; while doing so, the maximum electric field experienced by the metallic device should be kept bounded. Additionally, the transmit field homogeneity should be preserved.

If α is a vector of size, Nx1, whose elements are the complex currents on each channel of a TX array, the constraint on an electric field can be expressed by a linear equation, as follows:

$$E\alpha = c \qquad\qquad , (30)$$

where c, the desired electric field profile, is represented by a kx1 vector whose elements are equal to the desired electric field value at each point of interest, and E is a $k \, x \, N$ matrix. The elements of E at its ith column and j[th] row are equal to the value of the electric field at the jth sampling point obtained by exciting the ith array element with a unit current.

Similarly, the constraint on the transmit sensitivity can be expressed by the following linear equation:

$$B\alpha = d \qquad\qquad , (31)$$

where d, the desired transmit sensitivity profile, is represented by an $r \ x \ 1$ vector whose elements are equal to the desired transmit sensitivity at each point of interest and B is an $r \ x \ N$ matrix. The elements of at its ith column and j^{th} row are equal to the value of the transmit sensitivity at the jth sampling point obtained by exciting the ith array element with a unit current.

Average SAR can also be expressed as a function of α, as shown below:

$$SAR = \alpha^* R \alpha \qquad\qquad , (32)$$

where R is the electric field cross-correlation matrix with dimensions $N \ x \ N$. The element of R at its ith column and j^{th} row is equal to the correlation of electric fields generated by an ith and j^{th} coil, being both excited by a unit current. In order to minimize the average SAR, $\alpha^* R \alpha$ should be minimized by finding an optimum α, while keeping the electric field and sensitivity profile in the body under control. This requires solving an optimization problem in which all of these parameters are taken into account. The optimization problem can be expressed as follows:

$$
\begin{aligned}
&\min \ \alpha^* R \alpha \qquad\qquad . (32)\\
&0 \le E\alpha = c \le \varepsilon\\
&1 - \partial \le B\alpha = d \le 1 + \partial
\end{aligned}
$$

As the expressions above imply, the elements of d should be bounded at approximately 1, with an amount of ∂ that ensures homogeneity. In addition, the elements of c should be bounded between 0 and ε to reduce the RF heating of the metallic device. Lastly, among all of the solutions satisfying these constraints, the one with the minimum average SAR should be found.

5.4 Simulations

To verify the theory, simulation of an eight-channel transmit coil array (Figure 5.1) was performed at 123.7 MHz by using a simulation software FEKO [Version 9.3.24, Stellenbosch, SA].
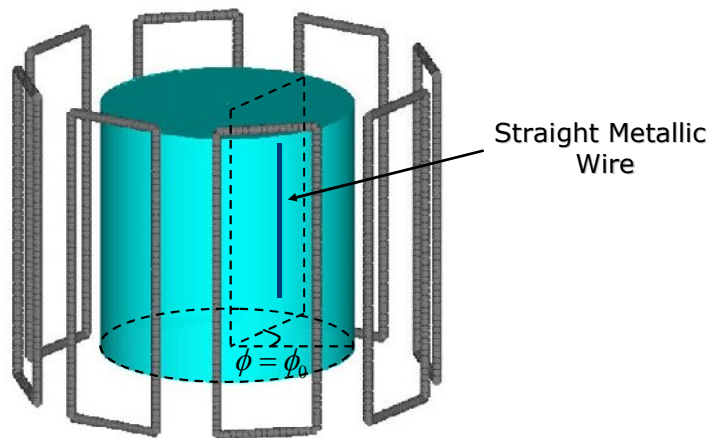

Figure 5.1 The uniform phantom model and transmit coil array used in the simulations. The conductivity, relative permittivity, and relative permeability of the medium is chosen as 0.5 S/m, 70, and 1, respectively.

The body was assumed as a homogenous cylinder with a diameter of 20 cm and a height of 30 cm. A straight metallic wire was assumed to exist in the body, 2 cm away from the boundary (Figure 5.1) located at the $\phi = \pi / 6$ plane. First, the quadrature field was used to excite the body model by using the current expression, $\alpha_i = \exp(2 \cdot \pi j \cdot i / N)$, where j is the imaginary number, $\sqrt{-1}$. Then, a linear field was used to excite the model. The excitation pattern for the coils was chosen as $\alpha_i = 2\sin(2 \cdot \pi i / 8 - \pi / 6)$ to reduce the RF heating of the device. Finally, the optimized currents were calculated for the SAR minimization. The elements of c were chosen such that the z component of the electric field was sampled at 7 points, separated by 3 cm along the wire. Similarly, the elements of d were chosen such that the transmit sensitivity was sampled at 45 points, distributed uniformly in the $z = 0$ plane. The simulations were made for two

values of ε, $\varepsilon = 3$ and $\varepsilon = 7$. In order to ensure that the transmit sensitivity did not vary more than 20 percent in the imaging plane, ∂ was chosen as 0.2.

In order to solve the optimization problem, a PSO [28] code was written in MATLAB (version 7.0, Mathworks Inc., Natick, MA). Because there was no closed-form solution of this optimization problem, the PSO method was implemented as in Chapter 2 to find the solution. The number of particles, the constriction factor, and the cognitive and social rates for velocity updates were chosen as explained in a previous work [40]. The fitness function was defined as the ratio of the average SAR value and the mean value of the transmit sensitivity in the imaging plane.

5.5 Results

The transmit sensitivity in the transverse plane for quadrature excitation, linear excitation and optimized excitations for $\varepsilon = 3$ and $\varepsilon = 7$ were calculated as seen in Figure 5.2.
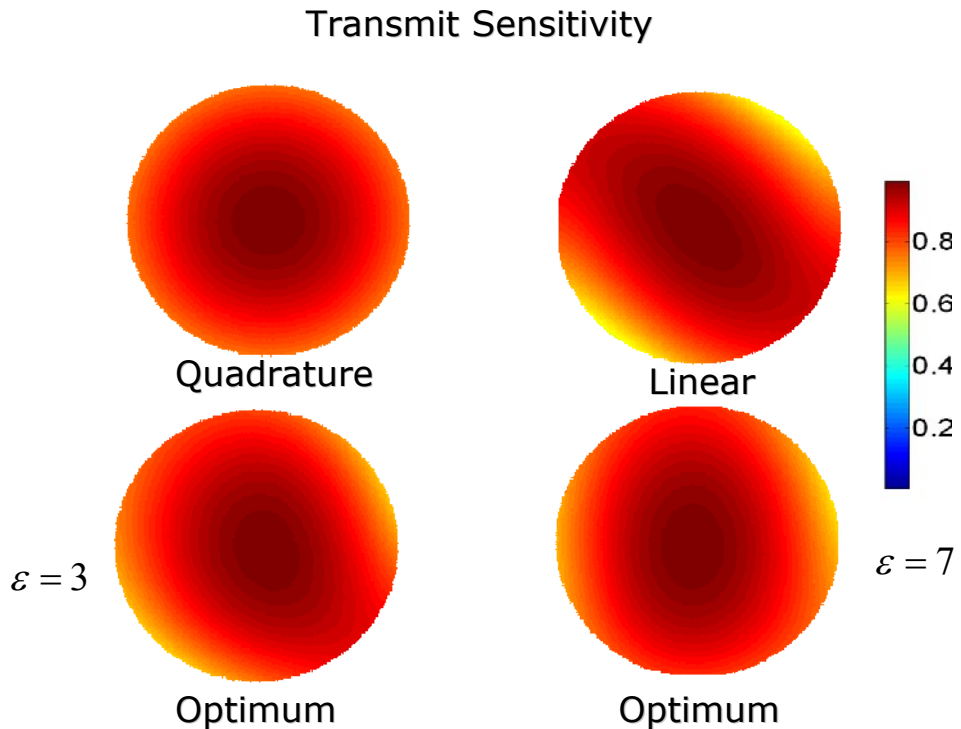

Figure 5.2 The transmit sensitivity solutions in the transverse plane due to the quadrature, linear and optimized excitations are shown.

As shown in Figure 5.2, the linear excitation resulted in a reduced transmit field homogeneity in the transverse plane when compared with the quadrature excitation. By using the optimum excitation currents, the homogeneity was improved with respect to the linear excitation.

The longitudinal component of the electric field was calculated and is shown in Figure 5.3.

Figure 5.3 The longitudinal component of the electric field due to the quadrature, linear and optimized excitations is shown in the transverse plane (the x marks the location of the straight metallic wire in the transverse plane).

By applying the optimum current patterns, the magnitude of the electric field was reduced significantly compared with quadrature excitation. However, a residual electric field whose value was limited by ε remained as expected. In contrast, the electric field along the metallic wire was completely reduced by using a linear excitation. A similar result can also be seen by examining the longitudinal electric field distribution in the angular plane, $\phi = \pi / 6$, shown in Figure 5.4. Note that the metallic wire was assumed to be confined in the $\phi = \pi / 6$ angular plane. The linear excitation completely reduced the electric

field in the entire $\phi = \pi / 6$ plane, while the optimized solution reduced the field only at sample points on the metallic wire.
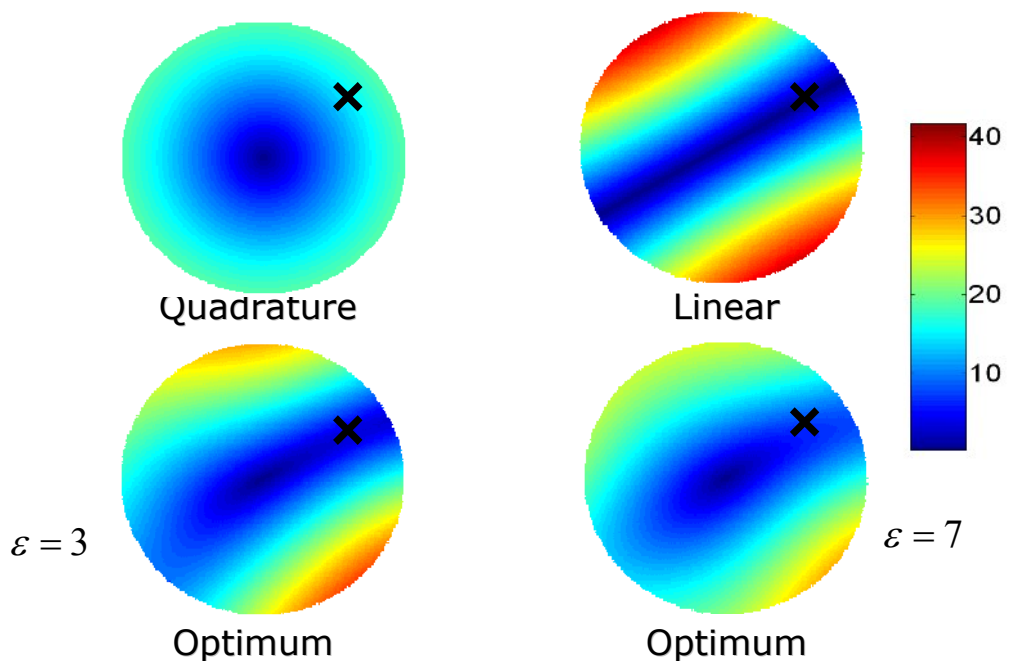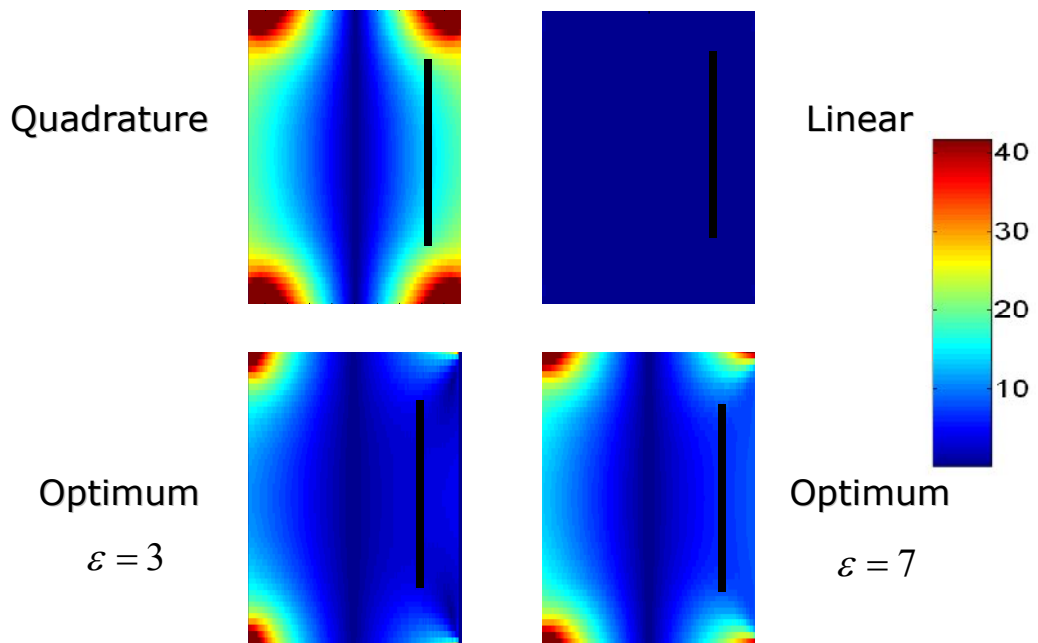

Figure 5.4 The longitudinal component of the electric field due to the quadrature, linear and optimized excitations, is shown in the in the angular plane, $\phi = \pi / 6$ (the location of the metallic wire is shown by a black straight line).

In Figure 5.5, the magnitude of the tangential component of the electric field is plotted along the metallic wire. The reduction in the electric field with respect to the quadrature excitation is clearly visible in the optimum solutions. With these solutions, it can also be noted from the same figure that the electric field magnitude remained under the ε threshold.
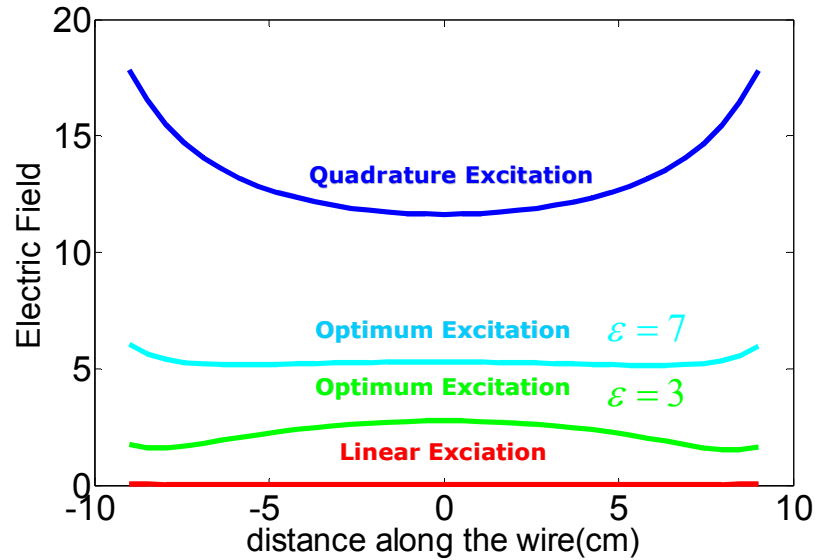
Figure 5.5 The variation of the tangential component of the electric field along the wire due to the quadrature, linear and optimized solutions is plotted.

Lastly, to compare the average SAR of the quadrature, linear, and optimum excitation currents, the SAR values were normalized by the mean value of transmit sensitivity in the imaging plane. As expected, the linear coil had an average SAR twice as the quadrature coil. The SARs due to the optimum excitations were 1.48 and 1.27 times the SAR of the quadrature excitation, whereas a reduction of 26% and 37%, with respect to linear excitation, was achieved by the optimum excitation currents with $\varepsilon = 3$ and $\varepsilon = 7$, respectively.

5.6 Discussions and Conclusions

In this work, it is shown that the electric field on the metallic devices can be reduced by modifying the electric field distribution using multi-channel transmit arrays. By controlling the currents on separate channels of the array, the local SAR around a metallic device can be reduced without sacrificing homogeneity or the average SAR.

69

The implementation of the method discussed in this chapter requires knowing several variables, including the electric field, transmit sensitivity and electric field cross-correlation matrices, namely E, B and R. In this work, they were calculated from simulations for a uniform phantom model. In real life, the transmit sensitivity for each channel can be measured in vivo by using different B1 mapping methods [41,42]. With recently developed techniques, it is possible to estimate the local variation of the electric field as well [43]. Another approach can also be adopted for this purpose based on measuring the induced current artifacts, as explained in Chapter 3. In such a case, a multi-channel excitation current pattern, which either cancels or limits the induced current on the metallic device, can be calculated. Because the current pattern should also satisfy the homogeneity and average SAR constraints, a similar optimization problem should be solved, as in the previous chapter. The electric field cross-correlation matrices can also be obtained in vivo by using the methods described in a previous publication [44].

6. THE EFFECT OF PHASE VARIATION OF THE ELECTRIC FIELD ON THE IMPLANT LEAD HEATING

6.1 Preface

A portion of the results that are presented in this chapter were published in a conference publication, reference: Eryaman Y. Acikel V, Abaci Turk E, Viskusenko N.V., Atalar E "Effect of Linear Phased Electric Field Variation On Implant Lead Heating" Proc Intl Soc Mag Reson Med 18(2010)**:**3894**.**

6.2 Introduction

In the previous chapters, it was shown that the magnitude of the electric field can be reduced in the vicinity of the metallic leads. This approach enabled the reduction of the RF currents that are induced on metallic devices. As a result, the local SAR near the tip of the device was substantially reduced. In this chapter, the effect of the phase distribution of the electric field on the RF heating is investigated. In a previous study [31], it was shown that the worst-case heating in metallic leads occurs when the phase of the electric field varies linearly along the lead. In that work, the local SAR at the tip of a metallic lead was maximized. In the work presented here, it is shown that the lead tip heating can also be reduced by varying the phase distribution along the implant lead. First, under quadrature excitation, it is demonstrated that a lead with a helical geometry experiences an incident electric field whose phase varies linearly along the lead. In that situation, a different amount of local SAR is generated at two tips of the helical lead. Due to the linear phase variation, the local SAR at one tip was significantly reduced with respect to the other one. Simulations and phantom experiments were conducted to demonstrate this effect. Second, it is demonstrated that the transmit arrays can be used to generate an incident electric field whose phase varies linearly along the lead. Similar to the case of a helical lead, a different amount of local SAR was generated at two tips of the lead.

6.3 Theory

In a previous study, the local SAR at the wire tip that is exposed to a linear phased electric field was calculated. [31]. In that study, the wire was divided into a number of segments, and the excitation of each segment was assumed to have an arbitrary phase. It was shown that a linear phase variation with a slope equal to the wave number, k, would cause a maximum constructive interference at a single tip, thus causing a maximum charge density at that tip. Because the local SAR near the implant tip increased with the square of the tip charge density, the heating was maximized.

As an extension of that result, the tip SAR can also be reduced by applying a linear-phased electric field excitation to a lead. As charge is accumulated due to constructive interference at one of the tips, destructive interference will cause a charge reduction at the other tip.

In Figure 6.1, a helical lead placed inside a uniform phantom is shown. A quadrature birdcage coil is used for the RF excitation. In such a case, a helical lead connecting the points A1 and B1 would experience an electric field whose phase would vary linearly along the lead.
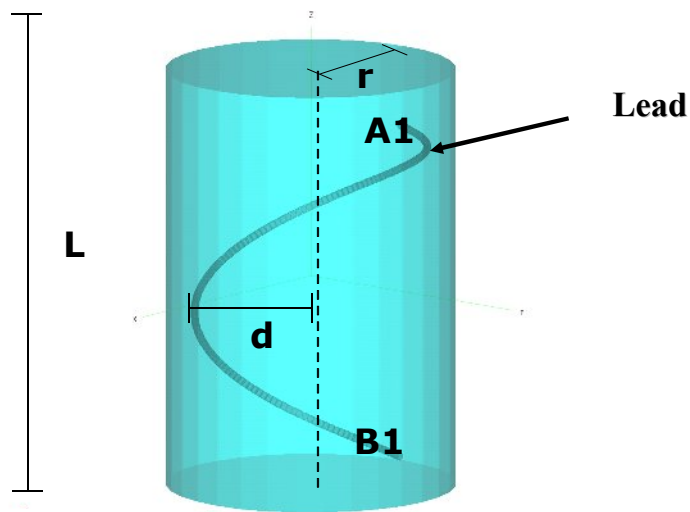
Figure 6.1 A lead with a helical geometry is placed inside a uniform head phantom model. The length and radius of the phantom, L and r, are chosen as 22 cm and 7.5 cm, respectively. The radius of the helix formed by the lead, d, is chosen as 6 cm.

The phase of the electric field of a quadrature birdcage coil varies linearly with respect to the angular direction. For that reason, the electric field along a helical lead, which is placed inside a birdcage coil to connect points A1 and B1, will also experience a linear phase variation. For a phase variation increasing in a counter-clockwise direction and a right-handed helical lead, the tip heating at point A1 would be expected to be more than the tip heating at point B1. For a left-handed helical lead, B1 would be expected to heat more than A1.

A condition similar to that explained above can also be obtained by using transmit arrays and a straight metallic wire, as in Figure 6.2. In such a case, the electric field variation along the lead has a phase determined by the phase of the excitation currents of the individual array elements. By introducing a phase to each array element, a linear phase variation can be obtained along the lead.

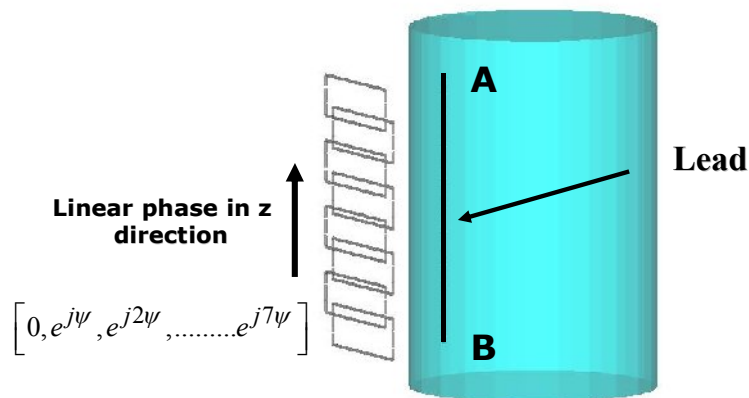$$\left[0, e^{j\psi}, e^{j2\psi}, \ldots\ldots e^{j7\psi} \right]$$

Figure 6.2 A straight lead inside the uniform phantom model is shown. The transmit array elements are fed by currents with same magnitudes but varying phases. With this method, an incident electric field is obtained whose phase is changing linearly along the lead.

With this method, the slope of the phase variation can also be controlled by controlling the excitation current phase, α.

6.4 Simulations and Experiments

The helical lead in Figure 6.1 was simulated by using the simulation software FEKO [Version 9.3.24, Stellenbosch, SA]. The leads were assumed to be placed in a cylindrical head model of radius 7.5 cm and length 22 cm. The conductivity and relative permittivity of the model were assumed as 0.5 S/m and 70, respectively. For excitation, a birdcage coil was simulated by assuming line current elements around the head model. The phase of each line current element varied linearly with respect to the angular location of the element.

In order to make a comparison, the phase of the tangential component of the electric field along the straight lead shown in Figure 6.3 was also simulated. Simulations were made for 1.5 T and 3.0 T. The SAR reduction at the tips of the helical leads was calculated with respect to the SAR at the tip of the straight lead.
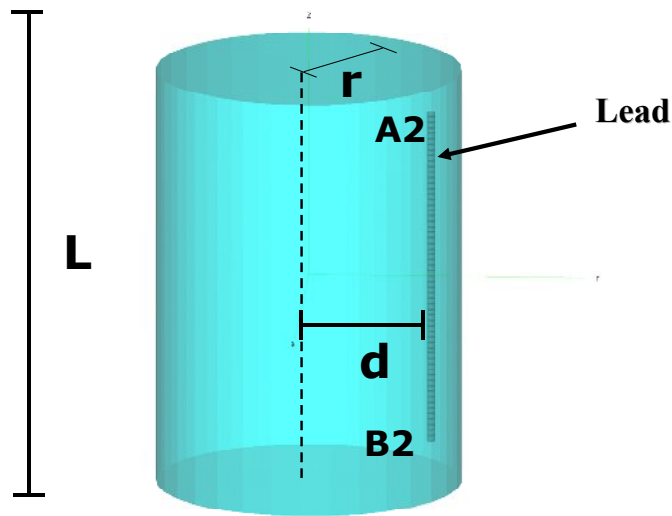
74

Figure 6.3 A straight lead inside the uniform head phantom model is shown. The lead is exposed to quadrature birdcage coil excitation.

In order to validate the simulation results, the phantoms with helical and straight leads shown in Figure 6.1 and Figure 6.3 were prepared by using a commercially available gel (Dr. Oetker Jello, Izmir, Turkey). To measure the conductivity and relative permittivity, a method based on cylindrical transmission line setup measurements was used. A conductivity of 0.5 S/m and a relative permittivity of 70 were obtained with 2.5 g/l of salt in the gel solution [36].

For 1.5 T, the phantoms were scanned with a GE Signa 1.5 T scanner by using a T/R head coil. An SPGR sequence with a flip angle of 90 degrees and TR of 6.25 msec was applied. For 3.0 T, the phantoms were scanned with a Siemens Tim Trio 3.0 T scanner by using the body coil. A GRE sequence with a flip angle of 90 degrees and a TR of 4.3 msec was applied.

For the temperature measurements, a signal conditioner (Neoptix ReFlex) with fiber optic temperature sensors (Neoptix Inc, Quebec City, Canada) was used. The temperature variations at the lead tips were recorded.

For the TX array, excitation of the straight lead and the phase and magnitude variations of the incident electric field along the lead were calculated for different α values. Then, the SAR reduction at tip A and the SAR amplification

at tip B were calculated with respect to the $\alpha = 0$ case. The SAR simulations were performed for both 1.5 T and 3.0 T.

6.5 Results

1.5 T
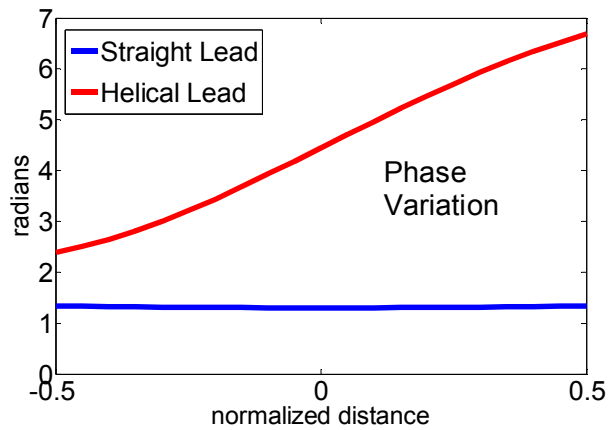
3.0 T
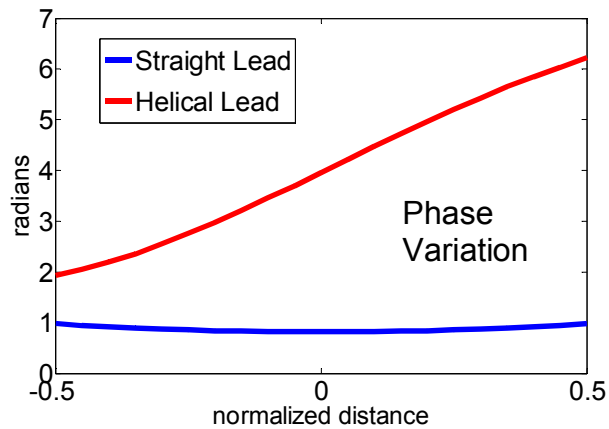
Figure 6.4 The phase variation of the electric field along the helical and straight leads is plotted.

The phase variations of the incident electric field along the helical and straight leads were calculated from the simulations (Figure 6.4). A quadrature birdcage coil model was used for the excitation. As expected, a constant phase was obtained for the straight lead, while an approximately linear phase variation was obtained for the helical leads. Although the phase was not perfectly linear, its effects on the lead tip SARs that were discussed in the theory chapter were expected to be present. The slope of the variation were almost identical for 1.5 T and 3.0 T. For the helical lead, the phase varied linearly with a slope of 8.8 rad/m for both of the field strengths.

The tip temperature measurements obtained from the 1.5 T experiments are shown in Figure 6.5. As depicted in the figure, the heating at tips A1 and B1 were different from each other. This was expected because the local SAR in tip A1 was more reduced when compared with tip B1. Furthermore, both tips of the helical lead heated less than the tip of the straight lead.
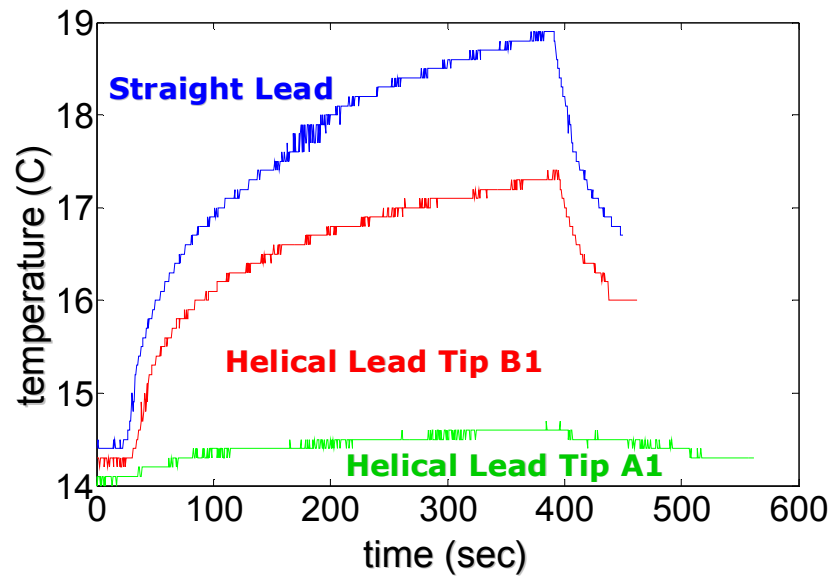

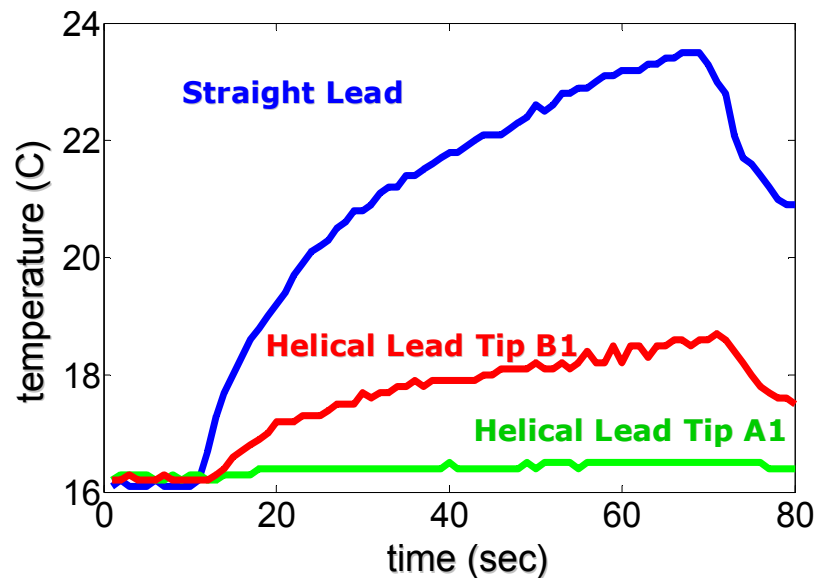Figure 6.5 The temperature variation recorded at the lead tips in 1.5 T.

Figure 6.6 The temperature variation recorded at the lead tips in 3.0 T.

Similar observations can also be made at 3.0 T by examining Figure 6.6. Both tips of the helical lead heated less in comparison with the straight lead, while the heating at tip A1 was more reduced. A quantitative local SAR comparison can be made by measuring the initial slope of the temperature curves. The local SAR reduction in the helical lead tips with respect to the straight lead tip was calculated. The reductions in the lead tip SAR were also calculated from the simulations. Table 1 shows the SAR reduction at tip A1 and tip B1 of the helical lead, with respect to straight lead, obtained from both the experimental and the simulation methods.

SAR Reduction with respect to straight lead

	Tip A1	Tip B1
1.5 T Simulation	%89	%50
1.5 T Experiment	%93	%39
3.0 T Simulation	%94	%64
3.0 T Experiment	%96	%69

Table 3 The SAR reduction at the tips of the helical lead with respect to straight lead is shown.

As shown in the table, the results obtained from the experiments and simulations are in agreement for both 1.5 T and 3.0 T.

In addition, the TX array in Figure 6.2 was simulated, and the phase variation of the incident field along the lead was calculated. The phase of the z component of the electric field was calculated for different α values, in a range of 0 to 90 degrees.
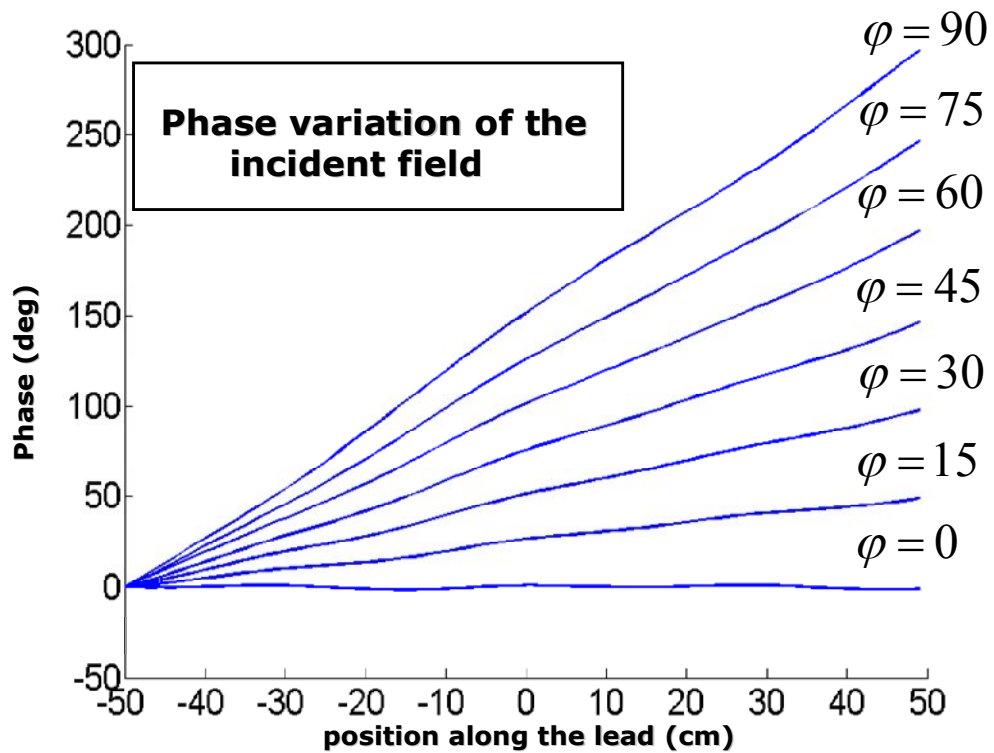
Figure 6.7 The phase variation of the incident electric field in 3.0 T is shown for different φ values.

As demonstrated in Figure 6.7, the transmit array excitation generated an incident electric field whose phase was approximately linear in the z direction. The slope of the variation also depended linearly on α.

Lastly, the SAR reduction at tip A and the SAR amplification at tip B were calculated, with respect to the $\alpha = 0$ case. The SAR simulations were made for both 1.5 T (Figure 6.8) and 3.0 T (Figure 6.9).
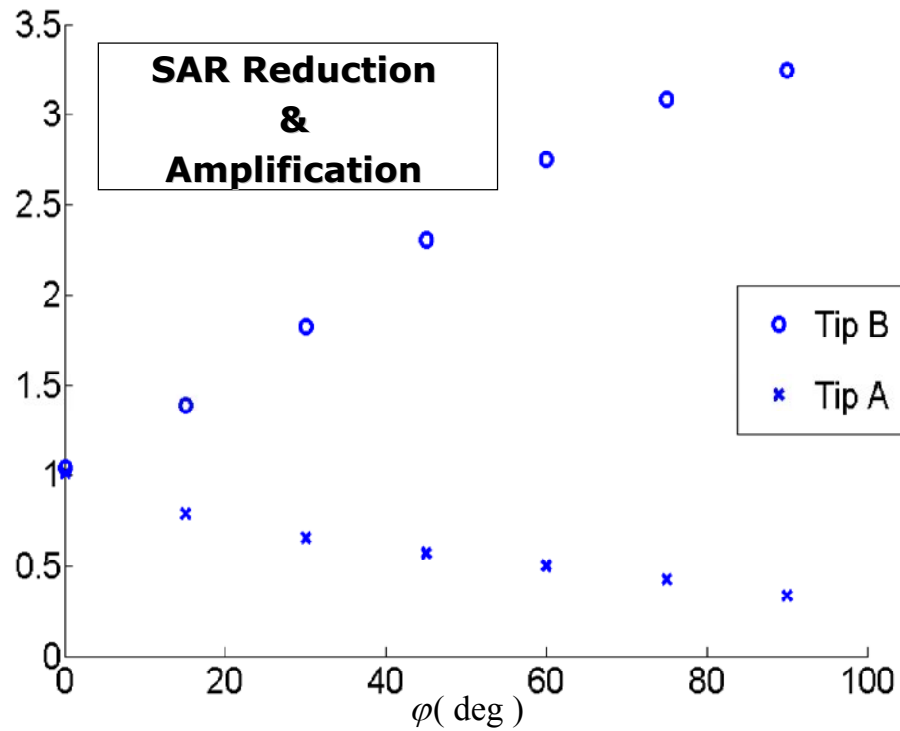
Figure 6.8. The SAR reduction in tip A and the SAR amplification in tip B with respect to the $\varphi = 0$ case are shown for 1.5 T.

As depicted in Figure 6.8 and Figure 6.9, the transmit array excitation reduced the SAR at tip A and amplified the SAR at tip B with respect to the $\alpha = 0$ scenario. For the range from 0 to 90 degrees for α, the larger variation in phase resulted in a larger reduction and amplification.
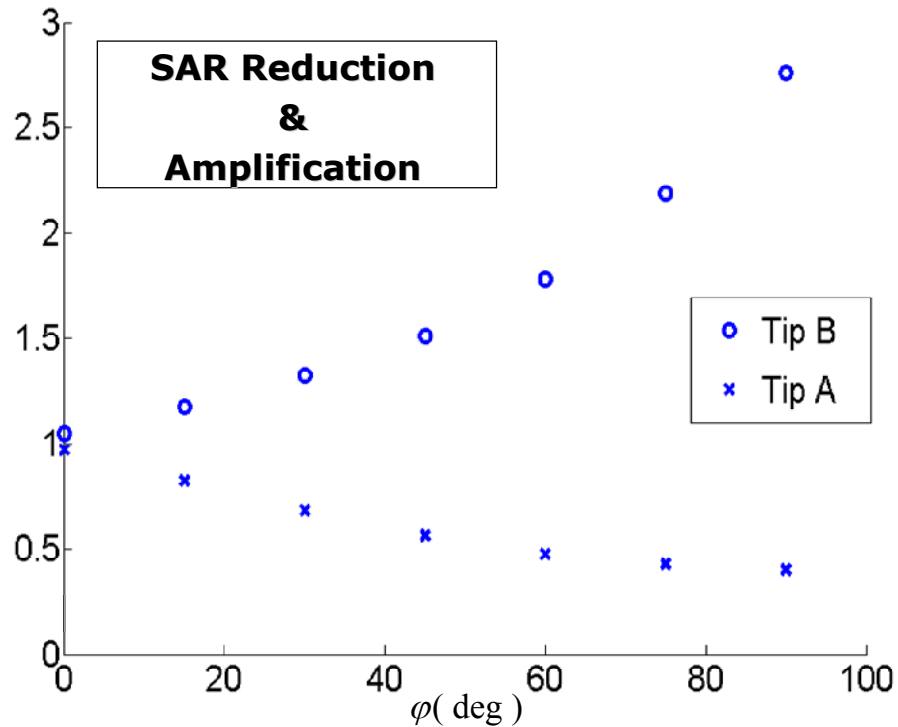
Figure 6.9 The SAR reduction in tip A and the SAR enhancement in tip B with respect to the $\varphi = 0$ case is shown for 3.0 T.

6.6 Conclusion

In this work, the effect of the phase variation of the incident electric field on the heating of metallic leads was demonstrated. When the leads were exposed to an incident electric field whose phase changed linearly along the lead, the local SAR at lead tips were substantially different. This effect was demonstrated with two methods. First, a helical lead inside a uniform phantom was exposed to quadrature excitation. The local SAR at the two tips of the helical lead was found to be different. The reduction in the local SAR with respect to a straight wire was also calculated. Second, a transmit array was used to excite a straight wire inside a uniform phantom. It was shown that the SAR was reduced at one tip and was enhanced at the other tip due to the phase variation of the electric field. The reduction and amplification in the SAR was calculated for different transmit array excitation patterns with respect to a zero phase excitation.

7. CONCLUSIONS

The methods that are proposed in this thesis can be used to improve the RF safety of patients during MRI. Modification of the spatial distribution of the electric field is the basis for the new methods that can be used to reduce the RF heating of human body. These methods can be applied to reduce both the average SAR and local SAR in the vicinity of the metallic devices. By realizing the optimum field solutions and designing appropriate transmitter coils average SAR can be reduced. As a result faster and safer scans can be performed at high field strengths. The methods related to the reduction of RF heating of metallic devices may improve the RF safety of MR guided interventional procedures and the scans performed on patients with implants.

Appendix

Derivation of Simplified Field Expressions

Cylindrical mode solutions of Maxwell's equations (45) can be used to express the EM field of birdcage coils. The total electric field is the summation of the cylindrical modes that are shown below (34):

$$E_{zmn} = A_{mn} J_m(\beta_{\rho n}\rho)e^{jm\phi}e^{-j\beta_{zn}z} \tag{33}$$

$$E_{\phi mn} = \left[\frac{A_{mn}}{\rho\beta}J_m(\beta_{\rho n}\rho) + \frac{\omega\mu}{\beta}B_{mn}J'_m(\beta_{\rho n}\rho)\right]e^{jm\phi}e^{-j\beta_{zn}z} \tag{34}$$

$$E_{\rho mn} = \left[\frac{B_{mn}}{\sigma'\rho}J_m(\beta_{\rho n}\rho) - jA_{mn}J'_m(\beta_{\rho n}\rho)\right]e^{jm\phi}e^{-j\beta_{zn}z} \tag{35}$$

$$H_{\rho mn} = \left[\frac{-m\beta^2 A_{mn}}{\omega\mu\rho\beta_{\rho n}{}^2}J_m(\beta_{\rho n}\rho) - \frac{\beta_{zn}B_{mn}}{\beta_{\rho n}}J'_m(\beta_{\rho n}\rho)\right]e^{jm\phi}e^{-j\beta_{zn}z} \tag{36}$$

$$H_{\phi mn} = \left[\frac{-jm\beta_{zn}B_{mn}}{\rho\beta_{\rho n}{}^2}J_m(\beta_{\rho n}\rho) - \frac{\sigma'A_{mn}}{\beta_{\rho n}}J'_m(\beta_{\rho n}\rho)\right]e^{jm\phi}e^{-j\beta_{zn}z} \tag{37}$$

where A_{mn} and B_{mn} are constants depending on the excitation, $J_m(x)$ is the Bessel function of order m and $J'_m(x)$ denotes the derivative of the mth order Bessel function. The forward and reversed polarized magnetic field components for transmission are defined as :

$$H_f = \frac{(H_\rho - jH_\phi)e^{-j\phi}}{\sqrt{2}}, \quad H_r = \frac{(H_\rho + jH_\phi)e^{j\phi}}{\sqrt{2}} \tag{38}$$

In the literature B1+ is used to refer to the transmit sensitivity of a coil. B1+ is defined in the rotating frame of reference. In our work we refer H_f as the transmit sensitivity. We solve our optimization problems by setting constraints on H_f which is defined in the phasor domain and proportional to B1+.

As a uniform transmit sensitivity is desired in a forward polarized birdcage coil, no "phi" and "z" dependences are desired. Therefore, the field can be approximated by using the cylindrical expansion mode with m=+1 and n=0. Similarly, m=-1 and n=0 can be used to approximate a reverse polarized birdcage coil. The modal expressions can be further simplified by using the following Bessel function approximations:

if $\beta\rho < 1$ then,

$$J_{-1}(\beta\rho) \approx -\frac{\beta\rho}{2}, \ J_1(\beta\rho) \approx \frac{\beta\rho}{2}, \ J_0(\beta\rho) \approx 1 \tag{39}$$

The approximate solutions for the forward polarized birdcage coil can be obtained as:

$$E_z = \frac{A\beta\rho}{2}e^{j\phi}, \ E_\phi = \frac{\omega\mu B}{2\beta}e^{j\phi}, \ E_\rho = \frac{-jB\omega\mu}{2\beta}e^{j\phi}, \ H_f = -\frac{A\beta}{\omega\mu_0}, \ H_r = 0 \tag{40}$$

Note that the $\beta\rho < 1$ condition implies that the radius of the object is much smaller than the wavelength. As can be seen in the expression of H_f, the transmit sensitivity is independent from the position of the coil. The constant B does not have any effects on the forward polarized magnetic field and only contributes to the electric field. Therefore, for the most efficient excitation (birdcage quadrature excitation), B should be equal to zero to minimize SAR, which results in the simplified expression of the following form:

$$E_z = \frac{-H_f\omega\mu_0\rho}{2}e^{j\phi}, \ E_\phi = 0, \ E_\rho = 0, \ H_f = -\frac{A\beta}{\omega\mu_0}, \ H_r = 0 \tag{41}$$

With the same approximations, field expressions of a reverse polarized birdcage coil can be expressed as:

$$E_z = \frac{H_f\omega\mu_0\rho}{2}e^{-j\phi}, \ E_\phi = 0, \ E_\rho = 0, \ H_f = 0, \ H_r = -\frac{A\beta}{\omega\mu_0} \tag{42}$$

By including the expressions of the forward and reverse polarized fields, one can express the approximate field components of a linear coil as:

$$E_z = -H_f j\omega\mu_0\rho\sin\phi, \ E_\phi = 0, \ E_\rho = 0, \ H_f = -\frac{A\beta}{\omega\mu_0}, \ H_r = -\frac{A\beta}{\omega\mu_0} \tag{43}$$

BIBLIOGRAPHY

1) International Standard, IEC 60601-2-33:2010

2) Setsompop K, Wald LL, Alagappan V, Gagoski B, Hebrank F, Fontius U, Schmitt F, Adalsteinsson E. Parallel RF transmission with eight channels at 3 Tesla. Magn Reson Med 2006; 56: 1163–1171.

3) Katscher U, Bornert P, Leussler C, van den Brink JS. Transmit SENSE. Magn Reson Med 2003; 49: 144–150.

4) Zhu Y. Parallel excitation with an array of transmit coils. Magn Reson Med 2004; 51: 775–784.

5) Metzger GJ, Snyder C, Akgun C, Vaughan T, Ugurbil, K. and Van de Moortele, PF Local B1+ shimming for prostate imaging with transceiver arrays at 7T based on subject-dependent transmit phase measurements. Magn Reson Med 2008; 59: 396–409

6) Lattanzi R, Sodickson DK, Grant AK, Zhu Y. Electrodynamic constraints on homogeneity and radiofrequency power deposition in multiple coil excitations. Magn Reson Med 2009;61(2):315-334.

7) Adriany G, Van de Moortele PF, Wiesinger F, Moeller S, Strupp JP, Andersen P, Snyder C, Zhang X, Chen W, Pruessmann KP, Boesiger P, Vaughan T, Ugurbil K. Transmit and receive transmission line arrays for 7 Tesla parallel imaging. Magn Reson Med 2005; 53: 434–445

8) Van den Berg CA, van den Bergen B, Van de Kamer JB, Raaymakers BW, Kroeze H, Bartels LW, Lagendijk JJ. Simultaneous B1 + homogenization and specific absorption rate hotspot suppression using a magnetic resonance phased array transmit coil. Magn Reson Med 2007; 57: 577–586.

9) Baker KB, Tkach JA, Nyenhuis JA, Phillips M, Shellock FG, Gonzalez Martinez J, Rezai AR. Evaluation of specific absorption rate as a dosimeter of MRI-related implant heating. J Magn Reson Imaging 2004;20(2):315-320.

10) Sommer T, Vahlhaus C, Lauck G, von Smekal A, Reinke M, Hofer U, Block W, Traber F, Schneider C, Gieseke J, Jung W, Schild H. MR imaging and cardiac pacemakers: in-vitro evaluation and in-vivo studies in 51 patients at 0.5 T. Radiology 2000;215(3):869-879.

11) Yeung CJ, Atalar E. A Green's function approach to local rf heating in interventional MRI. Med Phys 2001;28(5):826-832.

12) Yeung CJ, Susil RC, Atalar E. RF safety of wires in interventional MRI: using a safety index. Magn Reson Med 2002;47(1):187-193.

13) Henderson J. Permanent neurological deficit related to magnetic resonance imaging in a patient with implanted deep brain stimulation electrodes for Parkinson. Neurosurgey 2005:57

14) Heywang-Kobrunner, S. H., Heinig A, Pickuth D, Alberich T, Spielmann RP Interventional MRI of the breast: lesion localisation and biopsy. Eur Radiol 2000;10(1): 36-45.

15) Krieger, A., R. C. Susil, et al. (2005). "Design of a novel MRI compatible manipulator for image guided prostate interventions." IEEE Transactions on Biomedical Engineering 52(2): 306-313.

16) Worthley, S. G., G. Helft, et al. (2003). A novel nonobstructive intravascular MRI coil - In vivo imaging of experimental atherosclerosis. Arteriosclerosis Thrombosis and Vascular Biology 23(2): 346-350.

17) Nitz, W. R., A. Oppelt, et al. On the heating of linear conductive structures as guidewires and catheters in interventional MRI. Journal of Magnetic Resonance Imaging 2001 13(1): 105-114.

18) Ferhanoglu O, Eryaman Y, Atalar E. MRI Compatible Pacemaker Leads. Proc Intl Soc Mag Reson Med 2005;13:963.

19)Ladd ME, Quick HH. Reduction of resonant RF heating in intravascular catheters using coaxial chokes. Magn Reson Med 2000;43(4):615-619.

20)Gray RW, Bibens WT, Shellock FG. Simple design changes to wires to substantially reduce MRI-induced heating at 1.5 T: implications for implanted leads. Magn Reson Imaging 2005;23(8):887-891.

21)Bottomley PA,Kumar A,Edelstein WA,Allen JM,Karmarkar PV. Designing passive MRI-safe implantable conducting leads with electrodes. Med Phys 2010;37(7):3828-43

22) Hall A ,Martin A,Liu H,Truwitt C.L. Improving Diagnostic Yield in Brain Biopsy: Coupling Spectroscopic Targeting With Real-Time Needle Placement Magn.Reson Imaging 2001;13:12-15

23)Eryaman Y,Tunc.CA,Atalar E. Minimum SAR for RF Shimming by Allowing Spatial Phase Variation Proc Intl Soc Mag Reson Med 17(2009):

24)Eryaman Y, Akin B. Atalar E. Reduction of implant RF heating through modification of electric field Mag Reson Med 2010

25)Eryaman Y, Demir T, Atalar E Reduction of RF Heating of Metallic Devices Using Transmit Arrays Proc Intl Soc Mag Reson Med 18(2010):

26)Eryaman Y, Akin B,Oto C,Algin O,Atalar E Reduction of RF Heating of Metallic Devices by Using A Two-Channel Transmit Array System: Application to Arbitrary Lead Geometries Proc Intl Soc Mag Reson Med 19(2011):

27）Eryaman Y, Acikel V, Abaci Turk E ,Viskusenko N V, Atalar E Effect of Linear Phase Electric Field Variation on Implant Lead Heating Proc Intl Soc Mag Reson Med 18(2010):3894.

28)Robinson J, Rahmat-Samii Y. Particle Swarm Optimization IEEE Trans Ant Prop. 2004;52(2):397-407

29) Nordbeck P, Weiss I, Ehses P, Ritter O, Warmuth M, Fidler F, Herold V, Jakob PM, Ladd ME, Quick HH, Bauer WR. Measuring RF-induced currents inside implants: Impact of device configuration on MRI safety of cardiac pacemaker leads. Magn Reson Med 2009;61(3):570-578.

30) Nordbeck P, Fidler F, Weiss I, Warmuth M, Friedrich MT, Ehses P, Geistert W, Ritter O, Jakob PM, Ladd ME, Quick HH, Bauer WR. Spatial distribution of RF-induced E-fields and implant heating in MRI. Magn Reson Med 2008;60(2):312-319

31) Yeung CJ, Susil RC, Atalar E. RF heating due to conductive wires during MRI depends on the phase distribution of the transmit field. Magn Reson Med 2002;48(6):1096-1098.

32) Jin J, Chen J. On the SAR and field inhomogeneity of birdcage coils loaded with the human head. Magn Reson Med 1997;38(6):953-963.

33) Glover GH, Hayes CE, Pelc NJ, Edelstein WA, Mueller OM, Hart HR, Hardy CJ, O'Donnell M, Barber WD. Comparison of linear and circular polarization for magnetic resonance imaging. J Mag Res 1985;64(2):255-270.

34) Celik H, Eryaman Y, Altintas A, Abdel-Hafez IA, Atalar E. Evaluation of internal MRI coils using ultimate intrinsic SNR. Magn Reson Med 2004;52(3):640-649.

35) Ocali O, Atalar E. Ultimate intrinsic signal-to-noise ratio in MRI. Magn Reson Med 1998;39(3):462-473.

36) Akin B, Eryaman Y, Atalar E. A method for phantom conductivity and permittivity measurements. ESMRMB; 2009.

37) Vernickel P, Roschmann P, Findeklee C, Ludeke KM, Leussler C, Overweg J, Katscher U, Grasslin I, Schunemann K. Eight-channel transmit/receive body MRI coil at 3T. Magn Reson Med 2007;58(2):381-389.

38) Van den Bosch M. R., Moerland M. A., et al. New method to monitor RF safety in MRI-guided interventions based on RF induced image artefacts.2010 Med Phys 37(2): 814-821.

39) Etezadi-Amoli M, Stang P et al Controlling Induced Currents in Guidewires Using Parallel Transmit 2010 Joint Annual Meeting of ISMRM-ESMRMB

40)Clerc E, Keneddy J The particle Swarm Explosion,stability, and Convergence in a Multidimensional Complex Space IEEE Trans Evol, Comput Feb. 2002

41) Treier, R., Steingoetter, A., Fried, M., Schwizer, W. and Boesiger, P. (2007), Optimized and combined T1 and B1 mapping technique for fast and accurate T1 quantification in contrast-enhanced abdominal MRI. Magnetic Resonance in Medicine, 57: 568–576

42) Sacolick, L. I., Wiesinger, F., Hancu, I. and Vogel, M. W. (2010), B_1 mapping by Bloch-Siegert shift. Magnetic Resonance in Medicine, 63: 1315–1322

43) Katscher, U.; Voigt, T.; Findeklee, C.; Vernickel, P.; Nehrke, K.; Dossel, O.Determination of Electric Conductivity and Local SAR Via B1 Mapping, Medical Imaging, IEEE Transactions on , vol.28, no.9, pp.1365-1374, Sept. 2009

44) Deniz C. M., Alon L. Brown R., Fautz H-P., Sodickson D. K,Zhu Y. Real Time RF Power Prediction of Parallel Transmission RF Pulse Design at 7T Proc. Intl. Soc. Mag. Reson. Med. 18 (2010)

45) Foo TK, Hayes CE, Kang YW. An analytical model for the design of RF resonators for MR body imaging. Magn Reson Med 1991;21(2):165-177